SIMP Phase-field topology optimisation framework to maximise fracture resistance in FGMs.

Pavan Kumar Asur Vijaya Kumar[a,*], Pengfei Li[d,e], Jose Reinoso[b], Qi Chang He[d], Julien Yvonnet[d], Marco Paggi[c]

[a] *Institut für Leichtbau und Struktur-Biomechanik, Technische Universität Wien, Getreidemarkt 9, 1060 Vienna, Austria.*
[b] *Departamento de Mecánica de Medios Continuos y Teoría de Estructuras, School of Engineering, Universidad de Sevilla, Camino de los Descubrimientos s/n, 41092, Seville, Spain*
[c] *IMT School for Advanced Studies Lucca, Piazza San Francesco 19, 55100, Lucca, Italy*
[d] *Universitè Gustave Eiffel, MSME, CNRS UMR 8208, F-77454 Marne-la-Vallée, France*
[e] *School of Civil Engineering, Jiangsu Open University, Nanjing, 210036, China*

Abstract

In this study, we explore the use of SIMP topology optimization and the phase field approach to fracture to maximize fracture resistance in functionally graded materials (FGMs) in the presence of a second phase. We derive a mathematical formulation using a consistent derivation of the second law of thermodynamics to maximize the external work under the constraints of volume fraction. We also demonstrate that, for every distribution of the density function, the topology optimization problem $\Gamma-$Converges. We highlight the significant difference between the fracture resistance in FGMs and homogeneous materials. We investigate the crack propagation path along with the optimum topology for the FGM under different grading profiles, elastic mismatch ratio, strength mismatch ratio, and inclusion mismatch ratio. We present several numerical examples to demonstrate the predictive capability of the presented model. A comparison between the initial design guess and the final optimized design is also provided for each example, to further assess the model's capability.

Keywords: A.Topology Optimisation, B.Phase-field Method, C.Functionally Graded Materials, D.Finite Element Method, E. Fracture Resistance

1. Introduction

Functionally Graded Materials (FGMs) have gained notable popularity in the engineering community and industry [1] due to their ability to prevent interfacial stress concentration and improve fracture resistance [2]. FGMs are composed of two materials with spatial composition, which means that the material properties vary continuously within the specimen domain, typically by grading between two homogeneous constituents. This leads to a modified stress field and stress intensity factors, ultimately affecting the behavior of cracks in the material [3].

The crack propagation behavior in FGMs is fundamentally different from that in homogeneous materials [4, 5] and, therefore, can be especially complex. Numerous factors affect crack growth behavior, such as elastic mismatch [6], strength variations [7], geometry, residual stresses, grading laws, and more. Additionally, studies have shown that the crack propagation behavior can depend on the orientation of the crack relative to the grading profile [7–10]. Cracks oriented perpendicular to the grading profile experience asymmetric loading at the crack tip, which can lead to changes in crack propagation direction and induce mode mixity. On the other hand, grading parallel to the crack leads to straight propagation [7].

*Corresponding authors
Email address: pavan.kumar@ilsb.tuwien.ac.at (Pavan Kumar Asur Vijaya Kumar)

With recent advancements in 3D printing and additive manufacturing [11], it is possible to obtain on-demand geometries of multi-materials with desired structures. This has led to the exploration of new possibilities in the design of composites with enhanced functionalities, such as increased fracture resistance, suitable for applications in aircraft, automotive, and biomechanical engineering, among many others. Combining the advantages of 3D printing and additive manufacturing, topology optimization (TO) has become of extreme importance. TO has been widely studied and employed in both academic research and industrial applications since its invention [12].

Within this context, TO can be mainly categorized into three categories based on the optimization: 1) Solid Isotropic Material with Penalization (SIMP) [13–15], 2) level set method [16–19], and 3) evolutionary structural optimization (ESO) [20]. For a detailed review, see [16, 21–24]. TO can also be categorized based on the objective function, which includes 1) Minimization of compliance [22, 25–29], 2) Minimization of weight/volume [30], 3) Minimization of stress/energy [31–33], 3) position and shape of stiff inclusions [34–37] and 4) Maximization of fracture resistance [38–43].

The phase field method has recently advanced as an alternative tool for understanding nonlinear phenomena associated with cracks. Energy-based considerations in the phase field approach offer several advantages, such as the ability to predict crack nucleation and propagation, crack branching, and handling multiple cracks without any ad hoc methods [44]. This approach has been applied to brittle materials [45], ductile materials [46–48], composites [49–56], hydrogen-assisted cracking [57, 58], fatigue [59–62], and thermo-mechanical loadings [63–68]. The extensions of these models to functionally graded materials can be seen in [66, 69, 70]. For a detailed review of the phase field method, see [71].

TO has been employed in conjunction with the phase field to leverage its advantages. Specifically, the work in [34, 35, 72] extends TO to enhance fracture resistance in composites by considering both interfacial and bulk fracture. The analysis of full fracture initiation and propagation within the structure until failure [73] with BESO. In the case of composites, an extension to SIMP is presented in [14, 37, 74]. The optimization problem is formulated to minimize the total volume or volume and fracture energy while ensuring the fulfillment of the fracture energy dissipation constraint [75, 76]. Furthermore, a level set method based on TO is proposed for enhancing the brittle fracture resistance of two-phase composite materials [16, 17, 77]. Within the context of phase field, TO optimization has been used to find the optimum location of particles [78]. Recently, a solid mathematical foundation for maximizing fracture resistance in both ductile and brittle materials through the level set approach has been laid out in [79].

This work aims to achieve two objectives. The first objective is to present a mathematical foundation for maximizing fracture resistance within the context of the SIMP Phase field approach. It is demonstrated that the phase field formulation always $\Gamma-$converges for every distribution of the density function. The second objective is to apply the aforementioned formulation to functionally graded materials in order to increase their fracture resistance as a matrix and the third stiffer material as a second phase material (inclusion). Furthermore, the compliance and fracture resistance variations due to the topology optimization problem are compared to their homogenous surrogates to evaluate the potential of developing new materials with increased fracture resistance (as well as compliance) in this direction while taking into account volume constraints. It should be noted that the objective of this study is not to minimize the weight of the design but to obtain an optimal design under volume constraints in the case of compliance minimization and to modify the topology of the inclusion phase under the volume constraint.

The article is structured as follows. Section 2 presents a systematic mathematical formulation of topology optimization. Section 2.1 delves into the phase field formulation and its associated numerical methods. In Section 2.5, we discuss the $\Gamma-$Convergence of the problem. The Numerical Examples are divided into two parts. The first part (Section 3.1) explores the minimization of compliance for FGM using several representative examples without the phase field approach. The second part (Section 4) focuses on maximizing fracture resistance using the phase field approach with two representative examples. We consider a plate with a notch to investigate the effect of various factors on the topology optimization problem, including crack tips, elastic mismatch, strength mismatch, and inclusion ratio. An asymmetrical notch is used to evaluate the effect of asymmetry, the influence of grading, and the effect of grading on the crack path on the topology optimization problem. Both numerical examples are compared to their homogeneous surrogates to show the differences. Additionally, we evaluate the performance and capability of the proposed model in

the presence of an initial guess by considering several initial designs.

2. Mathematical Formulation

The objective of this section is to modify the topology under the constraint of volume fraction of a second phase material such that, for a prescribed load, mechanical work is maximised. For this, let $\Omega \subset \mathbb{R}^{ndim}$ ($ndim = 1, 2, 3$) be a body in $ndim$ Euclidean space $\mathbb{R}^{ndim}$ whose delimiting boundary is defined as $\partial\Omega \subset \mathbb{R}^{ndim-1}$. Let $\Gamma \subset \mathbb{R}^{ndim-1}$ be a crack set. The kinematic displacement of the body is characterised as a vector field $\mathbf{u}(\mathbf{X}, t) : \Omega \times [0, t] \to \mathbb{R}^{ndim}$ for all $\mathbf{x} \in \Omega$, and infinitesimal strain tensor $\boldsymbol{\varepsilon}(\mathbf{x}, t) : \Omega \times [0, t] \to \mathbb{R}^{ndim} \times \mathbb{R}^{ndim}$ defined as a symmetric gradient of the displacement field $\mathbf{u}$, i.e $\boldsymbol{\varepsilon}(\mathbf{x}) := \nabla^s \mathbf{u}(\mathbf{x})$, with $\nabla^s \mathbf{u} = \dfrac{\nabla \mathbf{u} + \nabla \mathbf{u}^T}{2}$. The external boundary is split into two disjoint sets, $\partial\Omega_E$ and $\partial\Omega_F$ such that $\overline{\partial\Omega_E \cup \partial\Omega_F} = \partial\Omega$, and $\partial\Omega_E \cap \partial\Omega_F = \emptyset$. Here, an external load is applied via prescribed displacement $\bar{\mathbf{u}}(\mathbf{x})$ for all $\mathbf{x} \in \partial\Omega_E$.

Here E and F are described as essential and free boundaries respectively. The external work $\mathcal{P}(\mathbf{u}(\mathbf{x}))$ due to the applied loading $\bar{\mathbf{u}}(\mathbf{x})$ takes the form

$$\mathcal{P}(\mathbf{u}(\mathbf{x})) := \int_{\Omega} \boldsymbol{f_v} \cdot \bar{\mathbf{u}} \, \mathrm{dV}, \tag{1}$$

where $\boldsymbol{f_v} : \Omega \to \mathbb{R}^{n_{dim}}$ is the body force/external force response for all $\mathbf{x} \in \Omega$, due to the load $\bar{\mathbf{u}}$, in $\mathbf{x} \in \partial\Omega_E$.

Define a scalar damage variable $\mathfrak{d} : \Omega \to [0, 1]$ such that $\mathfrak{d} = 0$ represents a intact material state, whereas $\mathfrak{d} = 1$ represents a fully broken state. Define a continuously differentiable density function $\rho(\mathbf{x}) : \Omega \to [0, 1]$ associated with inclusion phase, such that $\rho(\mathbf{x}) = 1$ denotes inclusion phase and $\rho(\mathbf{x}) = 0$ denotes matrix phase for all $\mathbf{x} \in \Omega$. Based on the existence of density function $\rho(\mathbf{x})$, the interior of the open set Ω is subdivided into three parts, namely (i) Ω_{inc} with $\rho(\mathbf{x}) = 1$ for all $\mathbf{x} \in \Omega_{inc}$, (ii)$\Omega_{mat}$ with $\rho(\mathbf{x}) = 0$ for all $\mathbf{x} \in \Omega_{mat}$, and (iii) Ω_{trans} with $\rho(\mathbf{x}) \in (0, 1)$ for all $\mathbf{x} \in \Omega_{trans}$, such that the union of these partitions make up the interior, and the domain do not overlap. This can be written as $\Omega_{mat} \cup \Omega_{inc} \cup \Omega_{trans} = \Omega$ and $\Omega_{mat} \cap \Omega_{inc} \cap \Omega_{trans} = \emptyset$.

The variational approach to fracture is seen as regularisation of the Griffith's energy potential. Within this context, the energy within the system can be seen as a competition between elastic energy $\Psi_u(\mathbf{u})$ created by external load and surface energy/ crack energy Ψ_S created due to creation of new surface. In this context, the quasi-static displacement $\mathbf{u}$ and the crack set Γ at any given discrete time instance $t \in [0, T]$ can be determined as the following minimisation problem

$$\Pi(\mathbf{u}, \Gamma) = \Psi_u(\mathbf{u}) + \Psi_S(\Gamma) - \mathcal{P}(\mathbf{u}(\mathbf{x})), \tag{2}$$

$$(\mathbf{u}_t, \Gamma_t) = \arg\min \Pi(\mathbf{u}, \Gamma)_{\mathbb{S}} := \int_{\Omega \setminus \Gamma} \Psi(\boldsymbol{\varepsilon}) \, \mathrm{dV} + G_C \mathcal{H}^{n_{dim}-1}(\Gamma \cap \overline{\Omega} \backslash \partial\Omega_t), \tag{3}$$

with $\mathbb{S} := [\mathbf{u} = \bar{\mathbf{u}} \, \mathrm{on} \, \partial\Omega_{\mathbf{u}}, \, \Gamma_t \supset \Gamma_{t-1}]$, $\mathcal{H}^{n_{dim}-1}(\Gamma)$ is the Hausdorff $(n_{dim} - 1)$ dimensional measure of crack set Γ, G_C is the critical energy release rate that depends on fracture toughness, and $\Psi(\boldsymbol{\varepsilon})$ is the elastic energy density which can be defined using constitutive relationship via strain field $\boldsymbol{\varepsilon}(\mathbf{x})$.

Due to the existence of density function, owing to topology optimisation framework, specifically SIMP approach, every material property is a function of density function. i.e

$$E(\rho) = \rho(\mathbf{x})^p E_{inc} + (1-\rho(\mathbf{x}))^p E_{mat}, \tag{4a}$$
$$G_C(\rho) = \rho(\mathbf{x})^p G_{C,inc} + (1-\rho(\mathbf{x}))^p G_{C,mat}, \tag{4b}$$
$$\Psi_u(\rho) = \rho(\mathbf{x})^p \Psi_{u,inc} + (1-\rho(\mathbf{x}))^p \Psi_{u,mat}, \tag{4c}$$
$$\tag{4d}$$

where E_{inc}, $G_{C,inc}$ are Youngs' modulus and energy release rate for the inclusion phase and E_{mat}, $G_{C,mat}$ are Youngs' modulus and energy release rate for the matrix phase. In general, $\Psi_{u,inc}$ and $\Psi_{u,mat}$ are the elastic energy associated with the inclusion and matrix phase respectively.

Notice that for all $\mathbf{x} \in \Omega_{inc}$, each function in Eq. (4) $F(\rho) = F_{inc}$, and for all $\mathbf{x} \in \Omega_{mat}$, the function $F(\rho) = F_{mat}$, and for $\mathbf{x} \in \Omega_{trans}$, the functions in Eq. (4) are linear/non-linear (depends on p) combinations of the properties of matrix and inclusion phase.

Hence, the total energy function is now density-dependent. Within the context of FGM, it is evident that the material properties exhibit a spatial variation within the specimen domain Ω. Assuming that the FGM is added only in the matrix phase, consider a grading profile $V_f = V_f(\mathbf{x})$, for all $\mathbf{x} \in \Omega|\Omega_{inc}$, all the material properties can be expressed as spatial variation, i.e $F_{mat} = F_{mat}(\mathbf{x}, V_f) = F_{mat}(\mathbf{x})$ for each material property F. Accomodating the functionally graded materials in the Eq. (4) leads to

$$E(\rho, \mathbf{x}) = \rho(\mathbf{x})^p E_{inc} + (1-\rho(\mathbf{x}))^p E_{mat}(\mathbf{x}), \tag{5a}$$
$$G_C(\rho, \mathbf{x}) = \rho(\mathbf{x})^p G_{C,inc} + (1-\rho(\mathbf{x}))^p G_{C,mat}(\mathbf{x}), \tag{5b}$$
$$\Psi_u(\rho, \mathbf{x}) = \rho(\mathbf{x})^p \Psi_{u,inc} + (1-\rho(\mathbf{x}))^p \Psi_{u,mat}(\mathbf{x}). \tag{5c}$$
$$\tag{5d}$$

Here, the functions $F_{mat}(\mathbf{x})$ is defined using volume fraction of the functionally graded materials. With this at hand, the total Griffith's energy in Eq. (3) can be defined as

$$\Pi(\mathbf{u}, \Gamma, \mathbf{x}, \rho) := \int_{\Omega \setminus \Gamma} \Psi(\boldsymbol{\varepsilon}(\mathbf{x}, \boldsymbol{\rho})) \, \mathrm{dV} + G_C(\mathbf{x}, \rho) \mathcal{H}^{n_{dim}-1}(\Gamma \cap \overline{\Omega} \setminus \partial\Omega_t). \tag{6}$$

For prescribed displacement load, maximizing the fracture resistance is equivalent to maximizing the mechanical work. For the applied load $\bar{\mathbf{u}}$ on $\partial\Omega_E$ whose external response is $F_{ext}(t)$, define the total mechanical work $J(\rho, \mathbf{u}, \Gamma)$

$$J(\rho, \mathbf{u}, \Gamma) = \int_0^t F_{ext}(s) \cdot \bar{\mathbf{u}}(s) \mathrm{ds}. \tag{7}$$

Then for each $t \in [0, T]$, with T corresponds to maximum loading time. i.e for $\bar{\mathbf{u}}(T) = \bar{\mathbf{u}}_{max}$, the topology optimisation problem can be described as

$$\text{Maximize:} \qquad J(\rho, \mathbf{u}, \Gamma), \tag{8a}$$
$$\text{Subjected to:} \quad \arg\min_{\mathbb{S}} \Pi(\mathbf{u}, \Gamma, \mathbf{x}, \rho) \quad \text{for each} \quad t \in [0, T] \tag{8b}$$
$$f^{inc} = \frac{V(\Omega_{inc})}{V(\Omega_{mat})} \leq \frac{C}{100}. \tag{8c}$$

with $\mathbb{S} := [\mathbf{u} = \bar{\mathbf{u}}\,\text{on}\,\partial\Omega_E,\ \Gamma_t \supset \Gamma_{t-1}\ \ , 0 \leq \rho(\mathbf{x}) \leq 1]$, for some constant C. Here $V(\Omega_{inc})$ is the volume defined as

$$V(\Omega) = \int_{\Omega} \rho(\mathbf{x}) \mathrm{dx}. \tag{9}$$

Notice that mechanical work is defined as a time integral, whereas energy minimisation problem is defined in a quasi-static setting. Hence, the energy minimisation problem has to be solved at every time step. Also, note that for this reason, the minimisation and the maximisation problems are not interchangeable.

Under the absence of crack Γ, the mechanical problem presented in Eq. (58) resembles that of the optimisation problem maximizing work with the inclusion phase.

2.1. Phase-field approximation

Since, Γ in the Eq. (58) is unknown a priori, numerical approximation of the function can be treated as Ambrosio-Torterelli elliptical regularization of the free discontinuity problem [80]. In this framework, the crack set Γ is replaced by a $(\mathcal{H}^{n_{dim}-1}, n_{dim}-1)$ rectifiable borel jump set of $\mathbf{u}$, $\bar{S}(\mathbf{u})$. Then a sequence of all C^1 hyper surfaces are used to cover the jump set $\bar{S}(\mathbf{u})$ by introducing a scalar damage variable $\mathfrak{d}$ (phase-field), such that the surface energy in Eq. (58) is approximated as

$$\Psi_S(\Gamma) = \int_{\Gamma} G_C(\rho, \mathbf{x}) \mathrm{ds} = G_C(\rho, \mathbf{x}) \mathcal{H}^{n_{dim}-1}(\Gamma \cap \overline{\Omega} \backslash \partial\Omega_t) \approx \int_{\Omega} \frac{G_C}{4c_w} \gamma(\mathfrak{d};\, \nabla\mathfrak{d})\ \mathrm{dV}, \tag{10}$$

where, $\gamma(\mathfrak{d};\, \nabla\mathfrak{d})$ is the crack surface energy density function defined as

$$\gamma(\mathfrak{d};\, \nabla\mathfrak{d}) := \frac{\alpha(\mathfrak{d})}{\ell} + \ell \left|\nabla\mathfrak{d}\right|^2. \tag{11}$$

Here, $c_w := \int_0^s \sqrt{\alpha(s)} ds$ is a normalizing parameter. $\alpha(\mathfrak{d})$ is a continuous monotonic function referred as geometric crack function that determines the distribution of phase-field model. $\ell \in \mathbb{R}^+$ is characteristic length scale that governs the width of the diffusive crack. The surface energy density function is equipped with a non-local part $\ell \left|\nabla\mathfrak{d}\right|^2$ that distinguish phase-field from the local damage theories.

Due to the phase-field approximation of Γ by $\mathfrak{d}$, the elastic energy is degraded using an energetic degradation function $g(\mathfrak{d}) : [0, 1] \to [1, 0]$ such that $g(0) = 1$, $g(1) = 0$, $\frac{dg}{d\mathfrak{d}} < 0$. i.e

$$\Psi_u(\mathbf{u}, \mathfrak{d}, \mathbf{x}, \rho) = \int_{\Omega} g(\mathfrak{d}) \Psi(\boldsymbol{\varepsilon}(\mathbf{u}), \mathbf{x}, \rho)\ \mathrm{dV}, \tag{12}$$

Then, the total regularised energy functional of the solid in Eq. (3) takes the form

$$\Pi_\ell(\mathbf{u}, \mathfrak{d}, \mathbf{x}, \rho) = \int_{\Omega} \left[g(\mathfrak{d})\right] \Psi(\boldsymbol{\varepsilon}, \mathbf{x}, \rho)\ \mathrm{dV} + \int_{\Omega} \frac{G_C(\mathbf{x}, \rho)}{4c_w} \left[\frac{\alpha(\mathfrak{d})}{\ell} + \ell \left|\nabla\mathfrak{d}\right|^2\right]\ \mathrm{dV} - \int_{\Omega} \boldsymbol{f_v} \cdot \bar{\mathbf{u}}\ \mathrm{dV}. \tag{13}$$

The thermodynamic consistency of the total energies can be ensured by considering rate dissipation of potential density function leading to Clausius-Duhem inequality

$$\dot{\mathcal{D}} = [\mathbf{S} - \partial_{\boldsymbol{\varepsilon}} \Pi_\ell] : \dot{\boldsymbol{\varepsilon}} - \partial_{\mathfrak{d}} \Pi_\ell : \dot{\mathfrak{d}} \geq 0. \tag{14}$$

Expanding the second term $\partial_{\mathfrak{d}} \Pi_\ell : \dot{\mathfrak{d}}$ leads to

$$\partial_{\mathfrak{d}}\Pi : \dot{\mathfrak{d}} = \left[-g'(\mathfrak{d})\frac{\partial\Psi(\boldsymbol{\varepsilon},\mathbf{x},\rho)}{\partial g} - G_C\left[\frac{\partial\gamma}{\partial\mathfrak{d}} - \nabla\cdot\frac{\partial\gamma}{\partial\nabla\mathfrak{d}}\right]\right] : \dot{\mathfrak{d}}.$$

In order for the Eq. (14) to hold, naturally $-g'(\mathfrak{d})\dfrac{\partial\Psi(\boldsymbol{\varepsilon},\mathbf{x},\rho)}{\partial g} \geq 0$, $\dot{\mathfrak{d}} \geq 0$, and $f_d(\mathfrak{d},\nabla\mathfrak{d}) \geq 0$ with

$$f_d(\mathfrak{d},\nabla\mathfrak{d}) = \left[-g'(\mathfrak{d})\frac{\partial\Psi(\boldsymbol{\varepsilon},\mathbf{x},\rho)}{\partial g} - G_C\left[\frac{\partial\gamma}{\partial\mathfrak{d}} - \nabla\cdot\frac{\partial\gamma}{\partial\nabla\mathfrak{d}}\right]\right] : \dot{\mathfrak{d}}. \tag{15}$$

The choice of functions $g(\mathfrak{d})$, $\alpha(\mathfrak{d})$ and $\Psi(\boldsymbol{\varepsilon},\mathbf{x},\rho)$ leads to the first order stability condition or often refereed to as KKT condition,

$$\dot{\mathfrak{d}} \geq 0; \qquad f_d(\mathfrak{d},\Delta\mathfrak{d}) \geq 0; \qquad f_d(\mathfrak{d},\Delta\mathfrak{d})\cdot\dot{\mathfrak{d}} = 0. \tag{16}$$

Here, $-g'(\mathfrak{d})\dfrac{\partial\Psi(\boldsymbol{\varepsilon},\mathbf{x},\rho)}{\partial g}$ is coined as energetic driving force. The choice of functions can be described as

1. The geometric crack density function $\alpha(\mathfrak{d}) = \mathfrak{d}^2$ is chosen so that phase-field problem renders linear within the staggered scheme.
2. The energetic degradation function $g(\mathfrak{d})$ degrades the equilibrium states satisfying $g(\mathfrak{d}) : [0,1] \to [1,0]$ takes the form

$$g(\mathfrak{d}) = (1-\mathfrak{d})^2. \tag{17}$$

3. The stored energy functional that describes the equilibrium state of the solid under load takes the form

$$g(\mathfrak{d})\Psi(\boldsymbol{\varepsilon},\mathbf{x},\rho) = g(\mathfrak{d})\Psi_0^+(\boldsymbol{\varepsilon},\mathbf{x},\rho) + \Psi_0^-(\boldsymbol{\varepsilon},\mathbf{x},\rho), \tag{18}$$

with

$$\Psi_0^{\pm}(\boldsymbol{\varepsilon}(\mathbf{x},\rho)) := \frac{1}{2}\lambda\langle tr(\boldsymbol{\varepsilon}(\mathbf{x},\rho))\rangle_{\pm}^2 + \mu\boldsymbol{\varepsilon}(\mathbf{x},\rho)^{\pm} : \boldsymbol{\varepsilon}(\mathbf{x},\rho)^{\pm}, \tag{19}$$

with λ and μ are standard lame parameter. Due to the polar decomposition theorem, strain tensor can be split written in terms of principle strains (eigenvalues) ε_n and the corresponding eigenvector $\mathbf{p}_n$ (for $n = 1,2,3$)

$$\boldsymbol{\varepsilon} = \sum_{n=1}^{3}\varepsilon_n\mathbf{p}_n\otimes\mathbf{p}_n = \boldsymbol{\varepsilon}^+ + \boldsymbol{\varepsilon}^-, \tag{20}$$

with positive and negative counterparts taking the form

$$\boldsymbol{\varepsilon}^+ = \sum_{n=1}^{3}\langle\varepsilon_n\rangle\mathbf{p}_n\otimes\mathbf{p}_n, \qquad \boldsymbol{\varepsilon}^- = \sum_{n=1}^{3} -\langle-\varepsilon_n\rangle\mathbf{p}_n\otimes\mathbf{p}_n, \tag{21}$$

with $\langle\varepsilon_n\rangle_{\pm} = \dfrac{1}{2}(\boldsymbol{\varepsilon}\pm|\boldsymbol{\varepsilon}|)$.

The solution to the total energy functional in Eq. (13) can be obtained by solving it as minimization problem:

Find, $(\mathbf{u}^*, \mathfrak{d}^*)$ such that

$$(\mathbf{u}^*, \mathfrak{d}^*) = \arg\min_{\mathbb{S}} \Pi_l(\mathbf{u}, \mathfrak{d}, \mathbf{x}, \rho), \tag{22}$$

with $\mathbb{S} := [\mathbf{u} = \bar{\mathbf{u}} \,\text{on}\, \partial\Omega_E,\ \dot{\mathfrak{d}} \geq 0]$ for a given density $\rho(\mathbf{x})$ distribution. Naturally, the set $(\mathbf{u}^*, \mathfrak{d}^*)$ in Eq. (22) can be obtained by taking the first variation of the total energy functional assuming enough regularity of the involved fields. For the admissible test functions $\delta\mathbf{u} \in \mathcal{B}^u$, and $\delta\mathfrak{d} \in \mathcal{B}^{\mathfrak{d}}$, the first variation leads to the following residual

$$\mathcal{R}_u(\mathbf{u}, \mathfrak{d}, \mathbf{x}, \rho, \delta\mathbf{u}) = \int_{\mathcal{B}_0} g(\mathfrak{d}) \left[\partial_{\boldsymbol{\varepsilon}} \Psi(\boldsymbol{\varepsilon}, \mathbf{x}, \rho) : \delta\boldsymbol{\varepsilon}(\mathbf{x}, \rho)\right] \, \mathrm{d}\Omega - \int_{\Omega} \boldsymbol{f_v} \cdot \delta\mathbf{u} \, \mathrm{dV} = 0, \tag{23}$$

for all $\delta\mathbf{u} \in \mathcal{B}^u$ with $\mathcal{B}^u = \{\delta\mathbf{u} \in \mathbf{H}^1(\Omega),\ \delta\mathbf{u} = 0 \text{ on } \partial\Omega_E\}$. The residual associated with the phase field problem takes the form

$$\mathcal{R}_{\mathfrak{d}}(\mathbf{u}, \mathfrak{d}, \mathbf{x}, \rho, \delta\mathfrak{d}) = \int_{\mathcal{B}_0} G_C \left[\frac{\mathfrak{d}}{\ell}\delta\mathfrak{d} + \ell\nabla\mathfrak{d} \cdot \nabla\delta\mathfrak{d}\right] \, \mathrm{d}\Omega - \int_{\mathcal{B}_0} 2(1-\mathfrak{d})\Psi(\mathbf{u}, \mathbf{x}, \rho)\delta\mathfrak{d} \, \mathrm{d}\Omega = 0, \tag{24}$$

for all $\delta\mathfrak{d} \in \mathcal{B}^u$, with $\mathcal{B}^{\mathfrak{d}} = \{\delta\mathfrak{d} \in H^1(\Omega) \big| \delta\mathfrak{d} \geq 0 \,\forall\, \mathbf{X} \in \Omega\}$. With this, the topology optimisation problem in Eq. (58) can be modified as

$$\begin{aligned}
&&\text{Maximize:} \quad && J(\rho, \mathbf{u}, \mathfrak{d}), && \text{(25a)}\\
\text{Subjected to:} \quad && \mathcal{R}^u = \mathcal{R}^{\mathfrak{d}} = 0 \quad && \text{for each} \quad t \in [0, T] && \text{(25b)}\\
&&&& f^{inc} = \frac{V(\Omega_{inc})}{V(\Omega_{mat})} \leq \frac{C}{100}. && \text{(25c)}
\end{aligned}$$

The residuals $\mathcal{R}^u$ and $\mathcal{R}^{\mathfrak{d}}$ can be solved using the well known finite element method.

2.2. Finite Element Discretization

Define discretization of the functional space Ω with n_e non-overlapping elements $\Omega = \approx \bigcup_{e=1}^{n_e} \Omega_{(e)}$ such that partition of unity holds. The discrete position is interpolated via standard trilinear shape function $\mathbf{N}(\boldsymbol{\xi})$ in local reference and as

$$\mathbf{X} \approx \sum_{I=1}^{8} N^I(\boldsymbol{\xi})\mathbf{X}_I = \mathbf{N}(\boldsymbol{\xi})\widetilde{\mathbf{X}},$$

for global vector $\widetilde{\mathbf{X}}$. The interpolation of the fields $(\mathbf{u}, \mathfrak{d})$ and their respective variations $(\delta\mathbf{u}, \delta\mathfrak{d})$ takes the form

$$\mathbf{u} \approx \mathbf{N}(\boldsymbol{\xi})\mathbf{d};\ \ \mathfrak{d} \approx \mathbf{N}(\boldsymbol{\xi})\tilde{\mathfrak{d}};\ \ \delta\mathbf{u} \approx \mathbf{N}(\boldsymbol{\xi})\delta\mathbf{d};\ \ \delta\mathfrak{d} \approx \mathbf{N}(\boldsymbol{\xi})\delta\tilde{\mathfrak{d}}.$$

The strain tensor $\boldsymbol{\varepsilon}$ and the gradient of the phase-field $\nabla_{\mathbf{x}}\mathfrak{d}$ are interpolated as

$$\boldsymbol{\varepsilon}^u \approx \mathbf{B}^{\mathbf{u}}\mathbf{d};\ \ \nabla_{\mathbf{x}}\mathfrak{d} \approx \mathbf{B}^{\mathfrak{d}}(\mathbf{d})\tilde{\mathfrak{d}},$$

where $\mathbf{B^u}$ and $\mathbf{B^\mathfrak{d}}$ are suitable gradient operators of the interpolation matrix $\mathbf{N}$. The discretization of the residuals results in the following discrete system of equations

$$\begin{bmatrix} \mathbf{K_u} & 0 \\ 0 & \mathbf{K_\mathfrak{d}} \end{bmatrix} \begin{bmatrix} \mathbf{d} \\ \mathfrak{d} \end{bmatrix} = \begin{bmatrix} \mathbf{F_u} \\ \mathbf{F_\mathfrak{d}} \end{bmatrix}, \tag{26}$$

with

$$\mathbf{K_u} = \int_\Omega g(\mathfrak{d}) \mathbf{B}^{u\,\mathrm{T}} \mathbb{C} \mathbf{B}^u \, \mathrm{d}\Omega; \quad \mathbf{K_\mathfrak{d}} = \int_{\mathcal{B}_0} \left[\frac{G_C}{\ell} \mathcal{H} \right] \mathbf{N}^\mathrm{T} \mathbf{N} \, \mathrm{d}\Omega + \int_{\mathcal{B}_0} G_C \ell \mathbf{B}^{\mathfrak{d}\,\mathrm{T}} \mathbf{B}^\mathfrak{d} \, \mathrm{d}\Omega, \tag{27}$$

where $\mathbb{C}$ is the undamaged elastic stiffness matrix, whereas the residual force vectors takes the form

$$\mathbf{F_u} = \int_\Omega \mathbf{N}^\mathrm{T} \cdot \boldsymbol{f_v} \, \mathrm{d}\Omega; \quad \mathbf{F_\mathfrak{d}} = \int_\Omega \mathbf{N}^\mathrm{T} \mathcal{H} \, \mathrm{d}\Omega. \tag{28}$$

2.3. Discrete Topology Optimisation

For each element density $\rho_e(\mathbf{x}) = \rho_1, \rho_2, \ldots \rho_{n_e}$, the discrete optimisation problem takes the form

$$\text{Maximize:} \qquad J^{\Delta \mathbf{u}}(\rho, \mathbf{u}, \mathfrak{d}), \tag{29a}$$

$$\text{Subjected to:} \qquad \mathcal{R}^u = \mathcal{R}^\mathfrak{d} = 0, \;\; (\mathbf{K}^n_\mathbf{u} \cdot \mathbf{d}^n = \mathbf{F}^n_\mathbf{u}, \;\; \mathbf{K}^n_\mathfrak{d} \cdot \mathfrak{d}^n = \mathbf{F}^n_{\mathfrak{d})} \qquad \text{for each} \qquad n = 1, 2, .., n_{load} \tag{29b}$$

$$\text{with} \quad f^{inc} = \frac{\sum_{e=1}^{N_e} \rho_e V_e}{\sum_{e=1}^{N_e} V_e}. \tag{29c}$$

for each $0 \leq \rho_e \leq 1$, for each element $e = 1, \ldots N_e$. Here, the superscript n refers to the n^{th} iteration with n_{load}. V_e is the volume of the e^{th} element. The external load function $J^{\Delta \mathbf{u}}$ in Eq. (29) can be approximated as

$$J^{\Delta \mathbf{u}} = \sum_{n=1}^{N_{load}} \Delta J^\mathbf{u} = \frac{1}{2} \sum_{n=1}^{N_{load}} (\mathbf{F}^n_{ext} + \mathbf{F}^{n-1}_{ext})^T \Delta \mathbf{u}^n, \tag{30}$$

where $\mathbf{F}_{ext}$ is the external load response at n^{th} step and $\Delta \mathbf{u}^n$ is the prescribed load increment at load step n.

2.4. Sensitivity Analysis

In order to solve the optimisation problem in Eq. (29), the sensitivity of the objective function $J(\rho, \mathbf{u}, \mathfrak{d})$ with respect to the design variable $\rho(\mathbf{x})$, $\dfrac{\partial J}{\partial \rho}$ must be determined. The sensitivity analysis is carried out using adjoint method via introduction of a Lagrangian

$$J^{\Delta \mathbf{u}} = \frac{1}{2} \sum_{n=1}^{N_{load}} (\mathbf{F}^n_{ext} + \mathbf{F}^{n-1}_{ext})^T \Delta \mathbf{u}^n + (\lambda^n_1)^T \mathcal{R}^n_u + (\lambda^n_2)^T \mathcal{R}^{n-1}_u + (\lambda^n_3)^T \mathcal{R}^n_\mathfrak{d} + (\lambda^n_4)^T \mathcal{R}^{n-1}_\mathfrak{d}, \tag{31}$$

where $\mathcal{R}_u$ and $\mathcal{R}_\mathfrak{d}$ are residuals as in Eqs. (23), (24) and superscript n and $(n-1)$ represents the load increments. Moreover $\mathbb{R}^{ndim} \ni \lambda_i$ for $i = 1, 2, 3, 4$ are Lagrangian multipliers.

Naturally, the sensitivity of the objective function J with respect to design variable $\rho_e(\mathbf{x})$ at elemental level takes the form

$$\frac{\partial J}{\partial \rho_e(\mathbf{x})} \approx \frac{1}{2} \sum_{n=1}^{N_{load}} \left[\frac{\partial (\mathbf{F}_u^n + \mathbf{F}_u^{n-1})^T}{\partial \rho_e} \Delta \mathbf{u}^n + (\lambda_1^n)^T \frac{\partial \mathcal{R}_u^n}{\partial \rho_e} + (\lambda_2^n)^T \frac{\partial \mathcal{R}_u^{n-1}}{\partial \rho_e} + (\lambda_3^n)^T \frac{\partial \mathcal{R}_\mathfrak{d}^n}{\partial \rho_e} + (\lambda_4^n)^T \frac{\partial \mathcal{R}_\mathfrak{d}^{n-1}}{\partial \rho_e} \right]. \quad (32)$$

The derivatives of the residuals at the equilibrium takes the form

$$\frac{\partial \mathcal{R}_\mathbf{u}^m}{\partial \rho_e} = \frac{\partial \mathbf{F}_\mathbf{u}^m}{\partial \rho_e} - \frac{\partial \mathbf{K}_\mathbf{u}^m}{\partial \rho_e} \cdot \mathbf{u}^m - \mathbf{K}_\mathbf{u}^m \cdot \frac{\partial \mathbf{u}^m}{\partial \rho_e}, \quad (33)$$

$$\frac{\partial \mathcal{R}_\mathfrak{d}^m}{\partial \rho_e} = \frac{\partial \mathbf{F}_\mathfrak{d}^m}{\partial \rho_e} - \frac{\partial \mathbf{K}_\mathfrak{d}^m}{\partial \rho_e} \cdot \mathfrak{d}^m - \mathbf{K}_\mathfrak{d}^m \cdot \frac{\partial \mathfrak{d}^m}{\partial \rho_e}. \quad (34)$$

Also, notice that due to external boundary conditions,

$$\frac{\partial \mathbf{u}^m}{\partial \rho_e} = \begin{cases} 0, & \text{for all } \mathbf{x} \in \partial\Omega_E \\ \dfrac{\partial \mathbf{u}_F^m}{\partial \rho_e}, & \text{otherwise} \end{cases}, \quad (35)$$

$$\frac{\partial \mathbf{F}_u^m}{\partial \rho_e} = \begin{cases} \dfrac{\partial \mathbf{F}_{u,E}^m}{\partial \rho_e}, & \text{for all } \mathbf{x} \in \partial\Omega_E \\ 0, & \text{otherwise} \end{cases}. \quad (36)$$

Hence,

$$\frac{\partial \mathbf{F}_u^m \cdot \Delta \mathbf{u}^m}{\partial \rho_e} = \frac{\partial \mathbf{F}_{u,E}^m}{\partial \rho_e} \Delta \mathbf{u}_E^m + \mathbf{F}_{u,F}^m \frac{\partial \Delta \mathbf{u}_F^m}{\partial \rho_e} = \frac{\partial \mathbf{F}_{u,E}^m}{\partial \rho_e} \Delta \mathbf{u}_E^m. \quad (37)$$

Now, with this at hand, the total work takes the form

$$\begin{aligned} \alpha_e = \frac{\partial J}{\partial \rho_e(\mathbf{x})} = \frac{1}{2} \sum_{n=1}^{N_{load}} & \frac{\partial \mathbf{F}_{u,E}^n}{\partial \rho_e} (\Delta \mathbf{u}_E^n + \lambda_{1,E}^n)^T + \frac{\partial \mathbf{F}_{u,E}^{n-1}}{\partial \rho_e} (\Delta \mathbf{u}_E^n + \lambda_{2,E}^n)^T + (\lambda_1^n)^T \left(\frac{\partial \mathbf{K}_u^n}{\partial \rho_e} \mathbf{u}^n + \mathbf{K}_u^n \frac{\partial \mathbf{u}^n}{\partial \rho_e} \right) \\ & - (\lambda_2^n)^T \left(\frac{\partial \mathbf{K}_u^{n-1}}{\partial \rho_e} \mathbf{u}^{n-1} + \mathbf{K}_u^{n-1} \frac{\partial \mathbf{u}^{n-1}}{\partial \rho_e} \right) - (\lambda_3^n)^T \left(\frac{\partial \mathbf{K}_\mathfrak{d}^n}{\partial \rho_e} \mathfrak{d}^n + \mathbf{K}_\mathfrak{d}^n \frac{\partial \mathfrak{d}^n}{\partial \rho_e} \right) - (\lambda_4^n)^T \left(\frac{\partial \mathbf{K}_\mathfrak{d}^{n-1}}{\partial \rho_e} \mathfrak{d}^{n-1} + \mathbf{K}_\mathfrak{d}^{n-1} \frac{\partial \mathfrak{d}^{n-1}}{\partial \rho_e} \right). \end{aligned} \quad (38)$$

Set $\lambda_{1,E} = -\Delta \mathbf{u}_E^n$ and $\lambda_{2,E} = -\Delta \mathbf{u}_E^n$ to eliminate the terms involving $\dfrac{\partial \mathbf{u}^n}{\partial \rho_e}$, the term $(\lambda_i \mathbf{K}_\mathbf{u})$ can be split into $\lambda_i \mathbf{K}_\mathbf{u} = \lambda_{iE} \mathbf{K}_{\mathbf{u},FE} + \lambda_{iF} \mathbf{K}_{\mathbf{u},FF}$. Then, choosing $\lambda_{1,F} = (\mathbf{K}_{\mathbf{u},FF}^n)^{-1} \mathbf{K}_{\mathbf{u},FE}^n \Delta \mathbf{u}_E^n$ and $\lambda_{2,F} = (\mathbf{K}_{\mathbf{u},FF}^{n-1})^{-1} \mathbf{K}_{\mathbf{u},FE}^{n-1} \Delta \mathbf{u}_E^{n-1}$, $\lambda_3 = \lambda_4 = 0$ leads to the following final objective derivative function.

$$\alpha_e = -\frac{1}{2} \sum_{n=1}^{N_{load}} \left\{ (\lambda_1^n)^T \frac{\partial \mathbf{K}_u^n}{\partial \rho_e} \mathbf{u}^n + (\lambda_2^n)^T \frac{\partial \mathbf{K}_u^{n-1}}{\partial \rho_e} \mathbf{u}^{n-1} \right\}. \quad (39)$$

Notice that, due to the choice of the function J defined in terms of mechanical work, the Lagrangian multipliers associated with phase-field, i.e λ_3 and λ_4 are null. In order to include the effect of the Phase-field variable, the objective function can be reformulated as

$$\tilde{J}^{\Delta \mathbf{u}} = \frac{1}{2} \sum_{n=1}^{N_{load}} \left\{ (\mathbf{F}_u^n + \mathbf{F}_u^{n-1})^T \Delta \mathbf{u}^n + (\mathbf{F}_\mathfrak{d}^n + \mathbf{F}_\mathfrak{d}^{n-1})^T \Delta \mathfrak{d}^n \right\}, \tag{40}$$

where sensitivity leads to the following final objective derivative function

$$\tilde{\alpha}_e = \frac{\partial \tilde{J}}{\partial \rho_e(\mathbf{x})} = -\frac{1}{2} \sum_{n=1}^{N_{load}} \left\{ (\lambda_1^n)^T \frac{\partial \mathbf{K}_u^n}{\partial \rho_e} \mathbf{u}^n + (\lambda_2^n)^T \frac{\partial \mathbf{K}_u^{n-1}}{\partial \rho_e} \mathbf{u}^{n-1} + (\lambda_3^n)^T \frac{\partial \mathbf{K}_\mathfrak{d}^n}{\partial \rho_e} \mathfrak{d}^n + (\lambda_4^n)^T \frac{\partial \mathbf{K}_\mathfrak{d}^{n-1}}{\partial \rho_e} \mathfrak{d}^{n-1} \right\}. \tag{41}$$

for each element e. Notice that $\dfrac{\partial J}{\partial \rho_e(\mathbf{x})}$ is a scalar quantity that indicate the sensitivity of the e^{th} element. The differences regarding the choice of the objective functions are explained in the sequel. Computationally, at each time step, if the sensitivity at $(n-1)$ step is known, then α_e^n is computed as

$$\alpha_e^n = \alpha_e^{n-1} + \Delta \alpha_e, \tag{42}$$

with

$$\Delta \alpha_e = (\lambda_1^n)^T \frac{\partial \mathbf{K}_u^n}{\partial \rho_e} \mathbf{u}^n + (\lambda_2^n)^T \frac{\partial \mathbf{K}_u^{n-1}}{\partial \rho_e} \mathbf{u}^{n-1} + (\lambda_3^n)^T \frac{\partial \mathbf{K}_\mathfrak{d}^n}{\partial \rho_e} \mathfrak{d}^n + (\lambda_4^n)^T \frac{\partial \mathbf{K}_\mathfrak{d}^{n-1}}{\partial \rho_e} \mathfrak{d}^{n-1}, \tag{43}$$

for each $n \in \{1, \ldots, n_{load}\}$. The instabilities such as checkerboard patterns are eliminated via smoothing the sensitivity α_e by means of filtering scheme, i.e.,

$$\alpha_e = \frac{\sum_{j=1}^{N_e} W_{ej} \alpha_j}{\sum_{j=1}^{N_e} W_{ej}}, \tag{44}$$

where the linear weight factor W_{ej} is defined as the non-negative distance between prescribed filter radius r_{min} and the element centre-to-centre distance $\Delta(e, j)$. i,e $W_{ej} = max(0, r_{min} - \Delta(e, j))$.

2.5. Γ-Convergence Analysis

The idea of this section is to show that for every distribution of the function $\rho(\mathbf{x})$, the phase-field approximation presented in this section $\Gamma-$converges. The details of the proof is now standard, hence only results are presented, whose detailed proof is a simple extension of the results in [80–83]. Due to the nature of topology optimisation framework presented in this article, the following assumptions can be made. The same notations as in [83] are used and detailed definitions are omitted here for the sake of brevity.

1. The displacement $\mathbf{u}$ is uniformly bounded in $L^\infty(\Omega; \mathbb{R}^{n_{dim}})$. i.e $\|\mathbf{u}\|_{L^\infty(\Omega; \mathbb{R}^{n_{dim}})} \leq M.$, for some constant M. Notice that the constant M can be easily defined as a function of applied displacement $\bar{u}$ on $\partial\Omega_E$.
2. Due to the definition of chosen energetic function and the split, assume $[u](\mathbf{x}) \cdot \upsilon \geq 0$, for $\mathcal{H}^{n_{dim}-1}$-a.e, $\mathbf{x} \in J_u$. This can be viewed as a linearized non-interpenetration condition due to the split [84]. Here, $[u](\mathbf{x})$ is the jump at $\mathbf{x}$ and υ is the normal to the jump at $\mathbf{x}$, which is wel defined in $\mathcal{H}^{n_{dim}-1}$-a.e on the jump set of $\mathbf{u}$, J_u.

Then, for any distribution $\rho(\mathbf{x})$, the total energy functional takes the form

$$\begin{aligned}\Pi_\ell(\mathbf{u},\mathfrak{d}) = \quad & \int_\Omega (\nu_l + (1-\mathfrak{d})^2)(2\mu(\mathbf{x},\rho)|\mathbf{E}^+(\mathbf{u})|^2 + \lambda(\mathbf{x},\rho)(Tr(\mathbf{E}^+(\mathbf{u}))^2) \\ & +(2\mu(\mathbf{x},\rho)|\mathbf{E}^-(\mathbf{u})|^2 + \lambda(\mathbf{x},\rho)(Tr(\mathbf{E}^-(\mathbf{u}))^2)\mathrm{d}\Omega \end{aligned} \tag{45}$$

$$+ \int_\Omega \frac{G_C(\mathbf{x},\rho)}{4}\left[\frac{\mathfrak{d}^2}{\ell} + \ell\,|\nabla\mathfrak{d}|^2\right]\,\mathrm{dV}. \tag{46}$$

Note that, ℓ can also be $\ell(\mathbf{x},\rho)$ can also be used, see [69] for more details. In this case, from Eq. (4) leads to $\ell(\rho) = \rho(\mathbf{x})^p\ell_{inc} + (1-\rho(\mathbf{x}))^p\ell_{mat}$. Let $\ell = min(\ell_{inc},\ell_{mat})$ without renaming the parameter that goes to zero, then $\ell_{inc} = \ell\cdot\tilde{C}_1$ and $\ell_{mat} = \ell\cdot\tilde{C}_2$, making ℓ_{mat}, ℓ_{inc} goes to zero as ℓ goes to zero.

The functional

$$\Pi_\ell^M(\mathbf{u},\mathfrak{d}) = \begin{cases}\Pi_\ell(\mathbf{u},\mathfrak{d}), & \text{if } \mathbf{u}\in H^1(\Omega;\mathbb{R}^{n_{dim}}), \mathfrak{d}\in H^1(\Omega;\mathbb{R}^{n_{dim}}), \|\mathbf{u}\|_{L^\infty(\Omega;\mathbb{R}^{n_{dim}})} \le M. \\ +\infty, & \text{otherwise}\end{cases}, \tag{47}$$

$\Gamma-$converges to

$$\Pi_0^M(\mathbf{u},\mathfrak{d}) = \begin{cases}\Pi_0(\mathbf{u}), & \text{if } \mathbf{u}\in SBD(\Omega), [u](\mathbf{x})\cdot\upsilon \ge 0, \mathcal{H}^{n_{dim}-1}-\text{a.e},\mathbf{x}\in J_u \\ +\infty, & \text{otherwise}\end{cases}, \tag{48}$$

as $\ell\to 0$, assuming $\lim_{\ell\to 0}\dfrac{\nu_l}{\ell} = 0$, with

$$\Pi_0(\mathbf{u}) = \frac{1}{2}\int_\Omega 2\mu|\mathbf{e}_d(\mathbf{u})|^2 + \lambda(Tr\mathbf{e}(\mathbf{u})^2)\mathrm{d}\Omega + G_C\mathcal{H}^{n_{dim}-1}(J_u). \tag{49}$$

The idea of the this proof is based on the fact that μ, λ and G_C do not play any role in the proof, but are scalars. By the definition of the decomposition of domain Ω, the domain Ω can be split into three parts based on the density function $\rho(\mathbf{x})$. i.e Ω_{inc}, Ω_{mat}, and Ω_{trans} such that the union of these partition make up Ω, and the domain do not overlap. This can be written as $\Omega_{mat}\cup\Omega_{inc}\cup\Omega_{trans} = \Omega$ and $\Omega_{mat}\cap\Omega_{inc}\cap\Omega_{trans} = \emptyset$. Note that since $\Omega_s = \{\Omega_{mat},\Omega_{trans},\Omega_{mat}\}$ is a closed set, and each of the set is bounded by the constant M from the L^∞ bound on $\mathbf{u}$, each set Ω_s is compact. Moreover, since Ω is the finite combination of the closed sets, Ω is closed as well. Then, the energies $\Pi_\ell^M(\mathbf{u},\mathfrak{d})$ can be defined as

$$\Pi_\ell^M(\mathbf{u},\mathfrak{d}) = \Pi_\ell^M(\mathbf{u},\mathfrak{d})\Big|_{\Omega_{inc}} + \Pi_\ell^M(\mathbf{u},\mathfrak{d})\Big|_{\Omega_{trans}} + \Pi_\ell^M(\mathbf{u},\mathfrak{d})\Big|_{\Omega_{mat}}. \tag{50}$$

From the definition of material properties as in Eqs. (4), (5), μ, λ, G_C are scalars. Moreover, due to the closed set Ω_s, the $H^1(\Omega_s;\mathbb{R}^{n_{dim}})$ and the jump sets takes the form J_u^s. Invoking the $\Gamma-$convergence results for each set individually, the following results can be readily seen

$$\Pi_\ell^M(\mathbf{u},\mathfrak{d}) = \begin{cases}\Pi_\ell^M(\mathbf{u},\mathfrak{d})\Big|_{\Omega_{inc}} + \Pi_\ell^M(\mathbf{u},\mathfrak{d})\Big|_{\Omega_{trans}} + \Pi_\ell^M(\mathbf{u},\mathfrak{d})\Big|_{\Omega_{mat}} & \text{if } \mathbf{u}\in H^1(\Omega_s;\mathbb{R}^{n_{dim}}), \mathfrak{d}\in H^1(\Omega_s;\mathbb{R}^{n_{dim}}), \|\mathbf{u}\|_{L^\infty(\Omega;\mathbb{R}^{n_{dim}})} \\ +\infty, & \text{otherwise}\end{cases} \tag{51}$$

$\Gamma-$converges to

$$\Pi_0^M(\mathbf{u},\mathfrak{d}) = \begin{cases} \Pi_0(\mathbf{u},\mathfrak{d})\Big|_{\Omega_{inc}} + \Pi_0(\mathbf{u},\mathfrak{d})\Big|_{\Omega_{trans}} + \Pi_0(\mathbf{u},\mathfrak{d})\Big|_{\Omega_{mat}} & \text{if } \mathbf{u} \in SBD(\Omega), [u](\mathbf{x})\cdot\upsilon \geq 0, \mathcal{H}^{n_{dim}-1} - \text{a.e,} \mathbf{x} \in J_u \\ +\infty, & \text{otherwise} \end{cases}, \tag{52}$$

as $\ell \to 0$, assuming $\lim_{\ell\to 0} \frac{\nu_l}{\ell} = 0$. Here, the Eq. (52) can be further expressed as

$$\Pi_0(\mathbf{u},\mathfrak{d})\Big|_{\Omega_{inc}} + \Pi_0(\mathbf{u},\mathfrak{d})\Big|_{\Omega_{trans}} + \Pi_0(\mathbf{u},\mathfrak{d})\Big|_{\Omega_{mat}} = \frac{1}{2}\int_\Omega 2\mu|\mathbf{e}_d(\mathbf{u})|^2 + \lambda(Tr\mathbf{e}(\mathbf{u})^2)\mathrm{d}\Omega + G_C(\rho,\mathbf{x})\mathcal{H}^{n_{dim}-1}(J_u^{inc}) \tag{53}$$

$$G_C(\rho,\mathbf{x})\mathcal{H}^{n_{dim}-1}(J_u^{trans}) + G_C(\rho,\mathbf{x})\mathcal{H}^{n_{dim}-1}(J_u^{mat}), \tag{54}$$

Notice that the sets Ω_s is compact. From the fine properties of the Hausdorff measure [81, 85], for every compact disjoint subsets Ω_i of Ω, for $i = \{1, 2, \dots n\}$, therefore positive distance from each other, we have

$$\sum_{i=1}^{n} \mathcal{H}^\alpha(\Omega_i) = \mathcal{H}^\alpha\left(\sum_{i=1}^{n}(\Omega_i)\right), \tag{55}$$

using the additivity of the Hausdorff measure, see [85, 86]. Hence, we have that

$$\mathcal{H}^{n_{dim}-1}(J_u^{inc}) + \mathcal{H}^{n_{dim}-1}(J_u^{trans}) + \mathcal{H}^{n_{dim}-1}(J_u^{mat}) = \mathcal{H}^{n_{dim}-1}(J_u^{inc} + J_u^{trans} + J_u^{mat}) = \mathcal{H}^{n_{dim}-1}(J_u). \tag{56}$$

which concludes the proof.

Remark: Notice that as $s \to \tilde{S}$ [of optimisation], due to the constraint $f^{inc} \leq C$, maximization of J can leads to limit case of $f^{inc} = C$, then $\Omega_{trans} \to \emptyset$, and $\Omega = \Omega_{inc} \cup \Omega_{mat}$, from definition, and $\rho(\mathbf{x})$ is binary.

3. Numerical experiments-without fracture

To obtain a comprehensive understanding of the behavior of functionally graded materials, this section has been divided into two distinct parts: topology optimization of compliance with FGM and SIMP topology optimization using phase field. These two sections serve different purposes.

Section 3.1, focuses on optimizing the topology of functionally graded materials to achieve minimum compliance while taking into account the available material constraints. On the other hand, Section 4, concentrates on maximizing the fracture resistance of the structure that consists of functionally graded materials and a homogeneous second phase material (inclusion) geometry. The formulation for this optimization approach is already presented in Section 2.

Both of these sections provide different insights into the behavior of functionally graded materials and their deisgn optimization, making them as a valuable contribution to the field of material engineering.

3.1. Minimization of compliance

In this section, the topology optimization problem under consideration is a simple modification that incorporates functionally graded materials (FGM) into a density-based approach. Each element e is associated with a density ρ_e and a volume fraction V_f, which determine the property of Young's modulus as:

$$E_e(\rho_e, V_f) = E_{min} + \rho_e^p(E(V_f) - E_{min}), \qquad \text{for } \rho_e \in [0,1]. \tag{57}$$

Here, $E(V_f)$ is defined as:

$$E(V_f) = E_1 + (E_2 - E_1) \times V_f(\mathbf{x}),$$

where E_1 and E_2 denote Young's modulus of homogeneous materials of one and two respectively, and $V_f(\mathbf{x})$ is the volume fraction function of the FGM at a given $\mathbf{x}$. The exponent p is typically set to $p = 3$ for compliance minimization problems, see [26, 27] for more details.

This modification allows for the incorporation of FGM into the optimization problem, providing a powerful tool for designing structures with enhanced mechanical properties. The mathematical formulation for minimum compliance problem takes the form

$$\text{minimise: } c(\mathbf{x}) = \boldsymbol{U^T K(x) U} = \sum_{e=1}^{N} U_e^T K_e(\mathbf{x}_e) U_e, \tag{58a}$$

$$\text{Subjected to: } \frac{V(\mathbf{x})}{V_0} = f(\mathbf{x}), \tag{58b}$$

$$\boldsymbol{K(x)U = F(x)}. \tag{58c}$$

In the above equations, c represents the total compliance, $\mathbf{U}$ and $\boldsymbol{F}$ are global displacement and force vectors, respectively, and $\boldsymbol{K(x)}$ is the global stiffness matrix that varies with the material properties over the domain $\mathbf{x} \in \Omega$.

It is important to note that the material properties $E(\rho_e, \mathbf{x})$ are constant for each element $\mathbf{x}_e$, i.e., $E(\rho_e, \mathbf{x}) = E_i$, where E_i depends on ρ_e and $\mathbf{x}$. Here, N is the total number of elements, $V(\mathbf{x})$ and V_0 are the material and design domain volumes, respectively, and f is a prescribed volume force.

To solve the optimization problem, the optimality criteria method is used along with the filtering method suggested in [27], we omit the details of the finite element analysis, construction of stiffness matrix, displacement and force vectors, and filtering schemes for the sake of brevity. Interested readers are encouraged to refer to [26, 27] for a detailed explanation of these concepts.

3.2. Half Three-point bending

In this section, the well-known half-three-point bending example is considered. For the sake of computational cost, only the right half of the asymmetric beam is considered with material properties $E_1 = 210$Gpa is fixed and E_2 is computed as $\dfrac{E_1}{E_2} = \mathcal{R}$. The domain is meshed with $200 \times 100\,(L \times W)$ in x- and y-direction. Here each mesh is considered to be the dimension of the domain as in the original problem [27]. The material property of Young's modulus is computed as

$$E(\mathbf{x}) = E_1 + (E_2 - E_1) * V_f(\mathbf{x}). \tag{59}$$

For the grading in x-direction, the volume fraction (of grading) tales the form

$$V_f(\mathbf{x}) = \left(\frac{x}{L}\right)^z,$$

where z is a grading constant. For the grading in the y-direction, the volume fractions of FGM take the form

$$V_f(\mathbf{x}) = \left(\frac{y}{W}\right)^z.$$

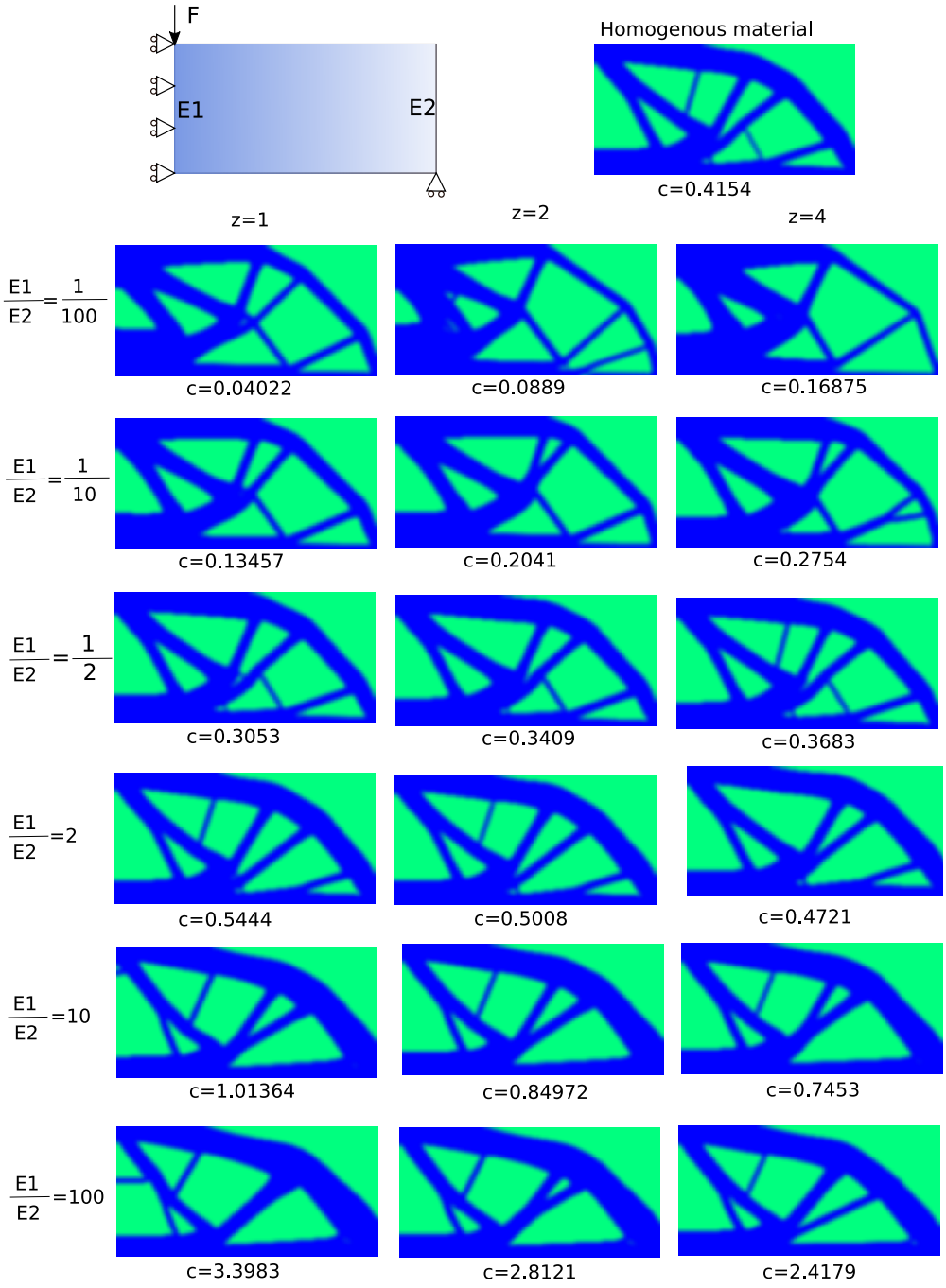

Figure 1: The Design domain, boundary conditions, external load for optimization of a symmetric MBB beam along with the optimised design for FGM with grading in x-direction for different grading profiles.

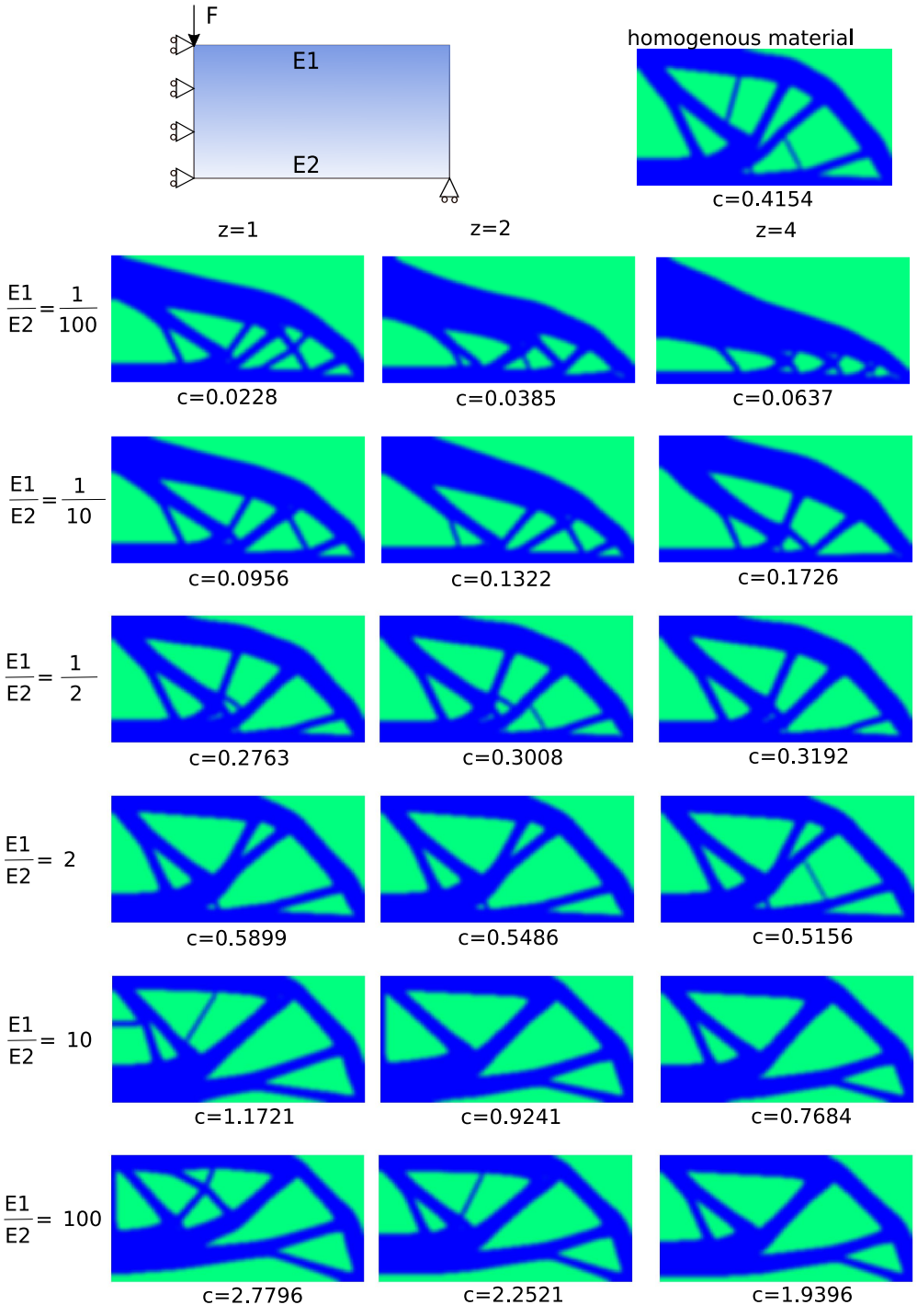

Figure 2: The Design domain, boundary conditions, external load for optimisation of a symmetric MBB beam along with the optimised design for FGM with grading in y-direction for different grading profiles.

Figure 1 presents the design domain boundary conditions, external load, and grading profiles in the x-direction. Additionally, the optimized designs for functionally graded materials (FGM) with various Young's modulus ratios of $\frac{E_1}{E_2} = \frac{1}{100}$, $\frac{1}{10}$, $\frac{1}{2}$, 2, 10, and 100 are presented, along with their variation of grading power $z = 1$, 2, and 4 along with the homogeneous optimized designs with a filter radius $R_{min} = 4$ and $f = 5\%$ are also included for comparison.

FGMs exhibit different behavior as compared to homogeneous materials. When $\frac{E_1}{E_2} < 1$, E_1 (left) has the lowest Young's modulus, and E_2 (right) has the highest. The optimum design for FGM is thicker towards the load application area (i.e., the side with the lowest Young's modulus), and the thickness requirement for the connecting strut decreases towards the highest Young's modulus side (E_2). For $\frac{E_1}{E_2} = \frac{1}{100}$, the left side ($E_1$ side) is the thickest, and the right side (E_2 side) is the thinnest. As the grading power z increases, this trend becomes more pronounced while increasing compliance. Furthermore, total compliance decreases as the $\frac{E_1}{E_2}$ ratio decreases and increases as z increases.

In other words, the compliance of the optimum design in FGM for $\frac{E_1}{E_2} < 1$ is directly proportional to the grading power z and inversely proportional to the $\frac{E_1}{E_2}$ ratio.

For $\frac{E_1}{E_2} > 1$, E_1 (left) has the highest Young's modulus, and E_2 (right) has the lowest. The reinforcement is required towards the right (E_2) side, whereas compromise and material towards the left (E_1) side can be made. This behavior is also reflected in the results presented in Fig 1. The compliance is directly proportional to $\frac{E_1}{E_2}$ and inversely proportional to z. i.e.,

$$c\ \alpha \left\{ \begin{array}{ll} \dfrac{z}{E_1/E_2}, & \text{for } \dfrac{E_1}{E_2} \leq 1 \\ \dfrac{E_1/E_2}{z}, & \text{for } \dfrac{E_1}{E_2} \geq 1 \end{array} \right\}. \tag{60}$$

Depending on the problem, the grading pattern can be selected to optimize the design. Figure 2 depicts the optimized design for the variation of $\dfrac{E_1}{E_2}$ ratio and z for the grading in the y-direction. As observed in the grading x-direction, when $\dfrac{E_1}{E_2} < 1$, E_1 (top) has the highest stiffness, whereas it has the lowest stiffness when $\dfrac{E_1}{E_2} > 1$. The existence of boundary conditions on the top right corner (external loading) and rolling support on the bottom right corner affects the optimum topology depending on the boundary conditions. For the case where $\dfrac{E_1}{E_2} < 1$, the structure is reinforced more towards the bottom as compared to the homogeneous solution. The opposite is observed when $\dfrac{E_1}{E_2} > 1$. The compliance follows the relation presented in Eq. (60), similar to the grading in the x-direction. The same methodology can be applied to obtain similar results for other structures. Appendix 7 provides examples of multi-objective topology optimization for half three-point bending with hole.

4. Topology optimisation of FGMs to fracture resistance

In this section, we present several two-dimensional examples to demonstrate the capacity, applicability, and convergence of the proposed method in maximizing fracture resistance. To highlight the similarities and differences between FGM and its homogeneous counterpart, two examples are considered for different purposes.

The first example involves a notched plate, and is used to investigate the effects of crack tips on design optimization, as well as the influence of grading and Young's modulus ratio $\dfrac{E_1}{E_2}$ and inclusion ratio $\dfrac{E_{inc}}{\max(E_1, E_2)}$. We also examine the differences between FGM and homogeneous solutions, and evaluate the

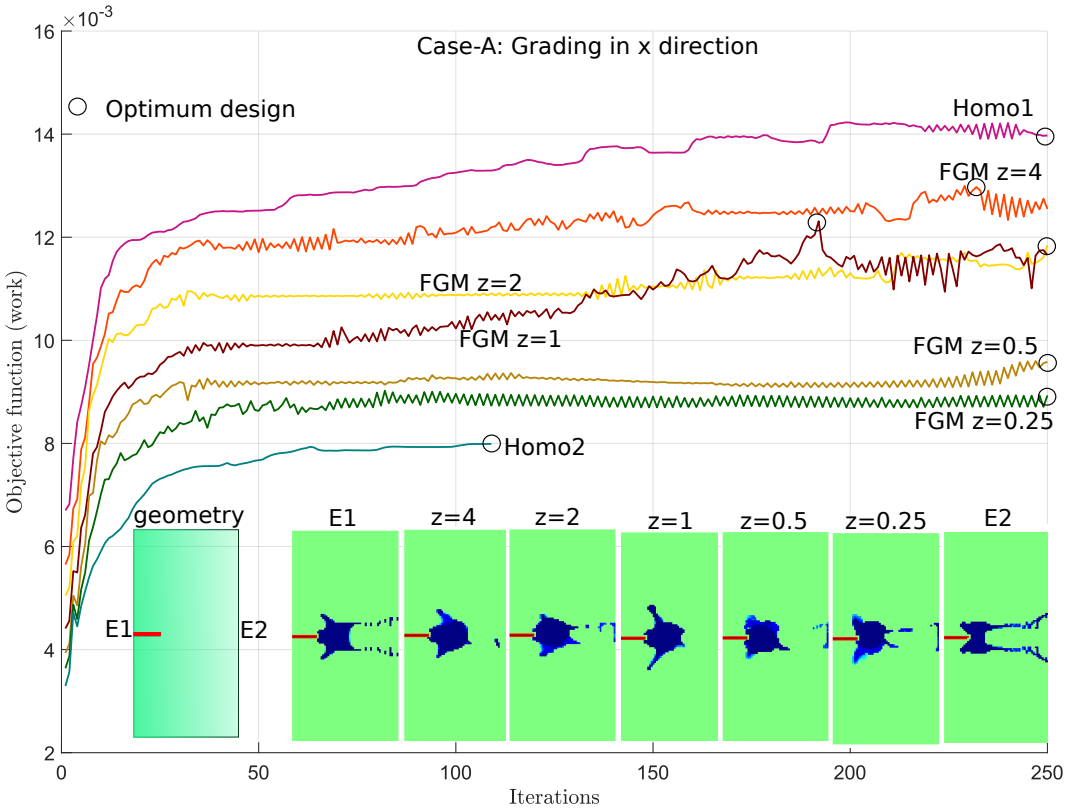

Figure 3: Grading in x-direction for 5 percent volume fraction of inclusion for Case-A

convergence of the topology optimization problem. Furthermore, we compare the FGM design obtained using the topology optmisation framework with the initial design guesses to demonstrate its superior design.

The second example concerns a plate with two asymmetrical notches, which is subjected to asymmetrical loading and crack propagation. We investigate the effect of asymmetry on design optimization, as well as the influence of grading and Young's modulus ratio. Additionally, we examine the effect of grading on the crack path.

In all numerical examples, we use quadrilateral bilinear elements with plane strain conditions. The phase field characteristic length scale ℓ is chosen to be twice the finite element size (h_e), in order to satisfy the mesh requirements in the phase field models, and the filter radius is set to $R_{min} = 2 * h_e$, i.e. twice the finite element size.

4.1. Plate with Notch

Crack propagation in FGMs differs significantly from homogeneous surrogates. Within this context, an initial characterization of the FGM can be based on two fundamental properties - (i) the Young's modulus ratio or elastic mismatch, and (ii) the apparent strength mismatch. Additionally, the characteristic length scale, ℓ, can also be considered a material property for FGM characterization. In this study, the characterization of the FGM is performed using (i) elastic mismatch, and (ii) apparent strength, while keeping ℓ constant. As the optimization problem focuses on maximizing fracture resistance by including a stiffer material (inclusion), the mismatch between the elastic properties of $\dfrac{E_1}{E_2}$ and the inclusion must be considered. The ratio of the highest Young's modulus of the FGM, $E' = \max(E_1, E_2)$, and the inclusion, $\dfrac{E_{inc}}{E'}$, is used

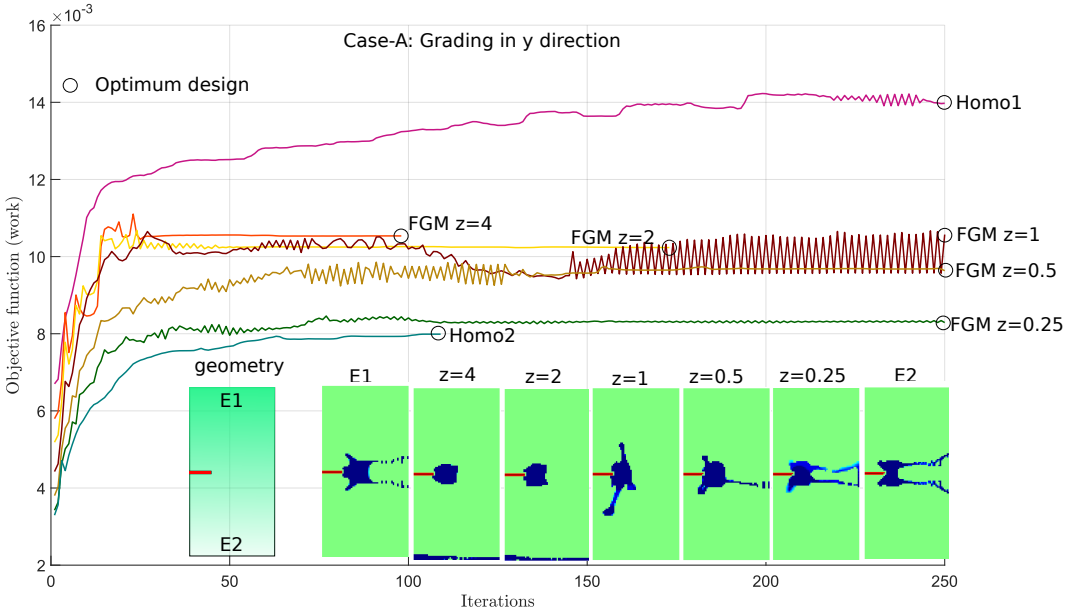

Figure 4: Grading in y-direction for 5 percent volume fraction of inclusion for Case-A

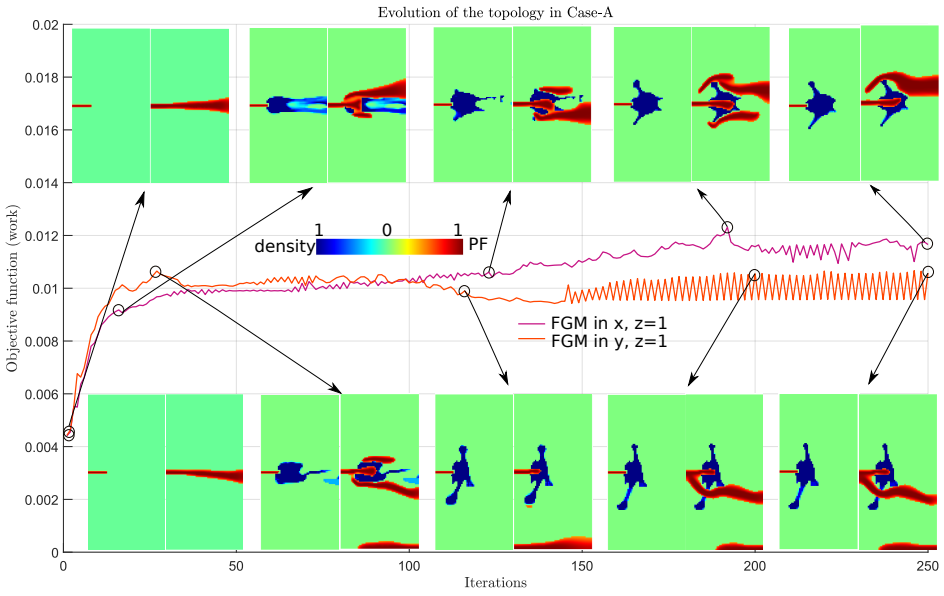

Figure 5: Evolution of the optimum topology in Case-A for the grading in X-direction and Y-direction for the volume fraction of 5% and $z = 1$ in y-direction for 5 percent volume fraction of inclusion.

Case	E_1	E_2	$\sigma_{c,1}$	$\sigma_{c,2}$	Elastic mismatch $\frac{E_1}{E_2}$	Inclusion mismatch $\frac{E_{inc}}{E'}$	Strength mismatch $\frac{\sigma_{c,1}}{\sigma_{c,2}}$	Inclusion strength mismatch $\frac{\sigma_{c,inc}}{\sigma'_c}$
Case-A	10.4	5.2	0.01	0.005	2	5	2	3
Case-B	5.2	10.4	0.005	0.01	0.5	5	0.5	3
Case-C	10.4	20.8	0.01	0.02	0.5	2.5	0.5	1.5

Table 1: Material properties and their corresponding mismatch ratios for different cases.

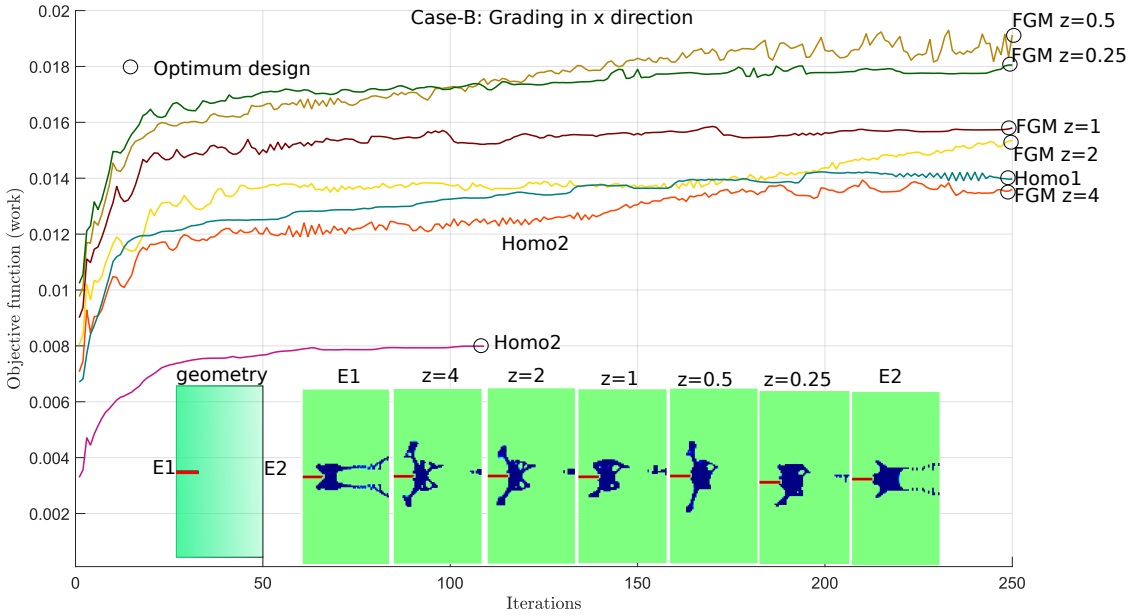

Figure 6: Grading in x-direction for 5 percent volume fraction of inclusion for Case-B

to characterize the FGM, referred to as the (iii) inclusion mismatch. A similar statement can be made about apparent strength to extract the (iv) inclusion strength mismatch [69, 70].

It should be noted that in the linear elastic regime, it is easy to prove that FGMs are bounded between their homogeneous surrogates in terms of both elastic energy and fracture energy [69]. In the case of plates with a notch, the length and placement of the crack can significantly affect the material response of FGMs. Therefore, we fix the geometry for the entire analysis. The geometry consists of a plate with dimensions of $L = 100$ mm and $W = 50$ mm, with a crack width of $W_c = 15$ mm placed at the center, as shown in Figure 3 (geometry). The model has been uniformly meshed with a 120×60 ($L \times W$) mesh, with finite element size $h_e = 0.833$. The initial density (ρ_0) across the domain Ω is set to be constant and equal to f^{inc}. During the entire optimization process, the volume fraction f^{inc} (of optimization) is fixed, while the densities ρ_e are allowed to evolve. The structure considered in this work is composed of an FGM material matrix made up of a combination of two homogeneous materials with properties E_1, E_2, $\sigma_{c,1}$, and $\sigma_{c,2}$, and we seek to find the optimal shape of an inclusion (with material properties E_{inc} and $\sigma_{c,inc}$) that provides the maximum fracture resistance for the entire composite structure. The pre-existing crack is enforced by prescribing a Dirichlet boundary condition of $\phi = 1$ along the crack.

For a comprehensive understanding of the impact of elastic mismatch, inclusion mismatch, and apparent strength mismatch, three different cases are examined. In each case, the inclusion properties are kept constant, with a Young's modulus of $E_{inc} = 52$ GPa and an apparent strength of $\sigma_{c,inc} = 0.03$ GPa.

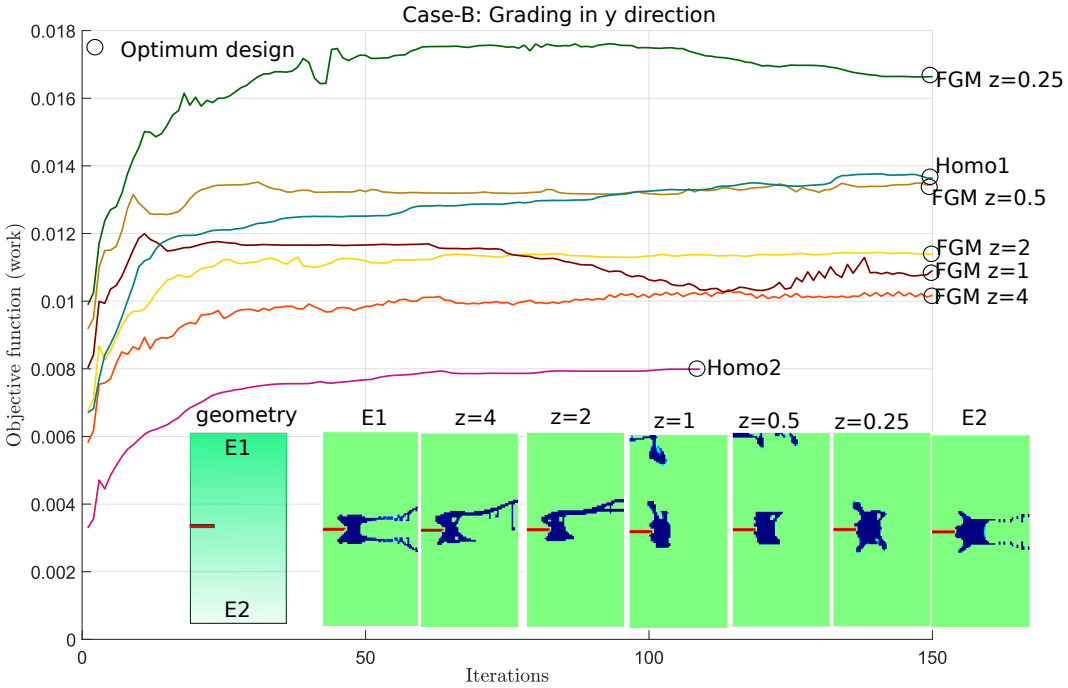

Figure 7: Grading in y-direction for 5 percent volume fraction of inclusion for Case-B

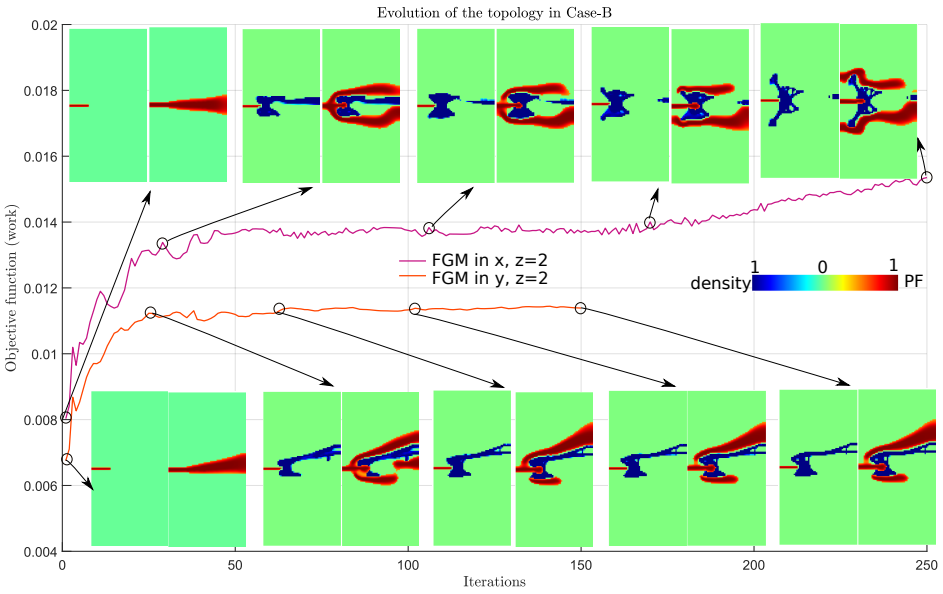

Figure 8: Evolution of the optimum topology in Case-B for the grading in X-direction and Y-direction for the volume fraction of 5% and $z = 2$ in y-direction for 5 percent volume fraction of inclusion

However, the matrix properties and their corresponding mismatch ratios are provided in Table 1 for each case.

It is worth noting that in all cases, E_1 is located on the left/top, and E_2 is located on the right/bottom for grading in the x-/y-directions, respectively. This affects the material properties at the crack tip and consequently, the crack propagation behavior, ultimately leading to changes in the optimal inclusion topology.

Figure 3 shows the iteration Vs. work for the grading in x-direction for case-A along with the optimum designs for FGM with $z = 4, 2, 1, \frac{1}{2}, \frac{1}{4}$ along with their homogeneous surrogates for $f^{inc} = 5\%$.

First, notice that E_1 has the highest Young's modulus, resulting in a decrease in resistance to fracture as we move away from the crack tip. As a consequence, inclusion densities are concentrated towards the crack tip to increase the stiffness of the crack propagation path.

It is easy to notice that, as $z \to \infty$, the grading of FGM resembles that of E_1, while as $z \to 0$, it behaves as E_2. It can be observed in Figure 3 that FGM's are sandwiched between their homogeneous constituents in terms of fracture resistance. However, the different resistance offered at the crack tip results in different optimum geometries for FGMs.

Figure 4 depicts the grading in the y-direction for Case-A, along with the optimum design for grading profiles with $z = 4, 2, 1, \frac{1}{2}, \frac{1}{4}$ and their homogeneous surrogates. In the y-direction, the properties at the crack tip along the line of the crack are nearly constant. However, the crack propagates towards the lowest Young's modulus side, i.e., E_2. Grading functions with $z = 4$ and $z = 2$ on the lowest Young's modulus side offer poor fracture resistance, necessitating the strengthening of the lowest E side in the optimum design. For the $z = 1$ case, the optimum design contains a leg that extends below due to the crack tending to go towards the bottom, increasing the fracture resistance by deviating the crack path. In the $z = \frac{1}{2}$ and $z = \frac{1}{4}$ cases, crack propagation tends to be less skewed compared to the other z's, but the optimum design is still dominated towards the lowest Young's modulus side. Additionally, the total work of FGM materials is sandwiched between their homogeneous surrogates in this case.

Figure 5 illustrates the evolution of optimum topology in Case-A for grading in the x- and y-directions, with $z = 1$. When graded in the x-direction, the crack propagates straight without any inclusion geometry, but later iterations demonstrate that the adjustment of density diverts the crack reaching an optimal topology with better fracture resistance. For the grading in the y-direction, crack propagation starts with a skewed crack towards the lowest Young's modulus side, slowly building inclusion densities around the less stiff areas to increase the fracture resistance during evolution.

Figures 6 and 7 show the iterations vs. work plots along with the optimum topology for FGM for Case-B with a volume fraction of $f^{inc} = 5\%$ in the x- and y-directions, respectively. Since E_1 is the side with the lowest Young's modulus, the resistance to fracture increases along the crack path for the grading in the x-direction. However, the initial crack also causes stress concentration, which forces the crack to grow towards the side with the highest Young's modulus. This competition is apparent in the optimum topology design in Figure 6. When $z = 4, 2$, the optimum design is more focused on enhancing the stiffness on the left side to avoid crack growth from the middle and close to the crack tip. For $z \leq 1$, stress concentration dominates, and the inclusion topology is more focused on preventing crack growth at the crack tip. Interestingly, FGMs offer more resistance in terms of work compared to their homogeneous surrogates in Case-B. This is readily seen in the iterations vs. work graph presented in Figure 6. A similar observation can be made for grading in the y-direction in Case-A, where the crack is propagated towards the side with the lowest Young's modulus (upper). In this case, only $z = 0.25$ performs better than its homogeneous surrogates, whereas the other FGMs are sandwiched between the homogeneous solutions. Comparing Case-A and Case-B, an improvement in terms of work can be readily seen in both x- and y-direction grading. The evolution of the optimum topology for grading in both x- and y-directions for $z = 2$ is shown in Figure 8.

A similar analysis can be conducted for Case-C. Due to its similarity to Case-B, with the only differences being inclusion mismatch and apparent inclusion mismatch, small differences in results can be obtained and are presented in Appendix 8. For the sake of brevity, the analysis is omitted.

Given the improved performance in Case-B, the optimum topology for grading in the x- and y-directions for volume fractions of $f^{inc} = 10\%$ and $f^{inc} = 15\%$ for $z = 2, 1$, and $\frac{1}{2}$ are presented in Figure 9. The homogeneous solution for $f^{inc} = 10\%$ is also presented for reference.

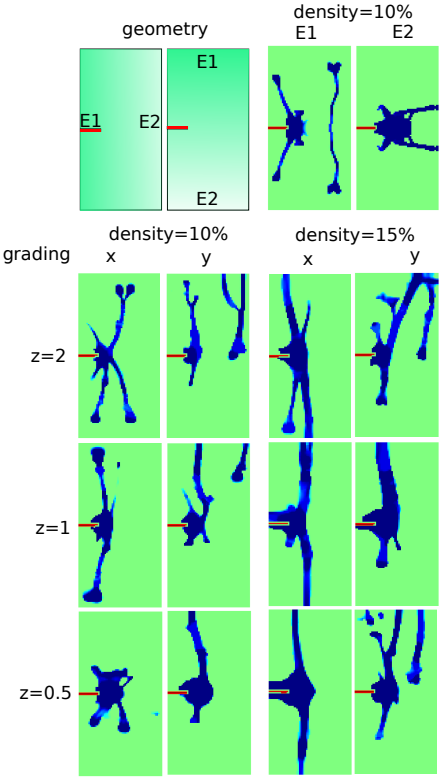

Figure 9: Optimum topology in Case-B for the grading in X-direction and Y-direction for the volume fraction of 10%, and 15% for the variation of the $z = 2, 1, 0.5$ along with their homogeneous solutions with 10% volume fraction of densities.

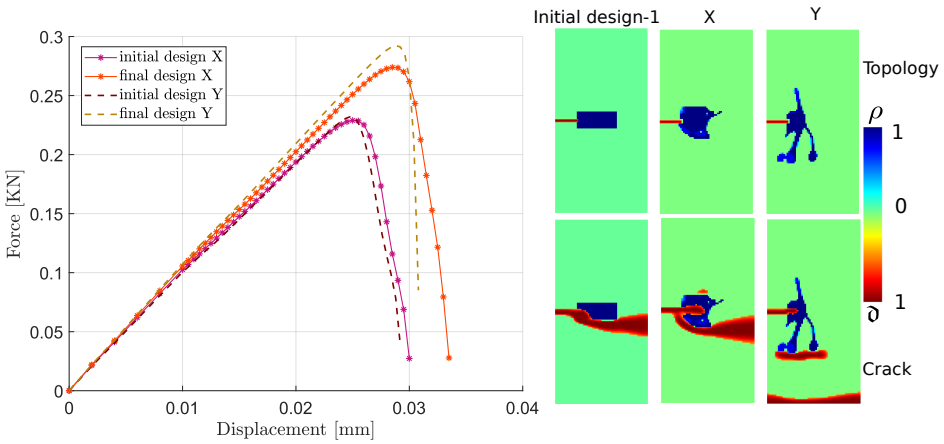

Figure 10: a) Force Vs. displacement of Design-1 with improved performance for Case-A, and b) Final optimum solution from the initial design along with the corresponding crack propagation.

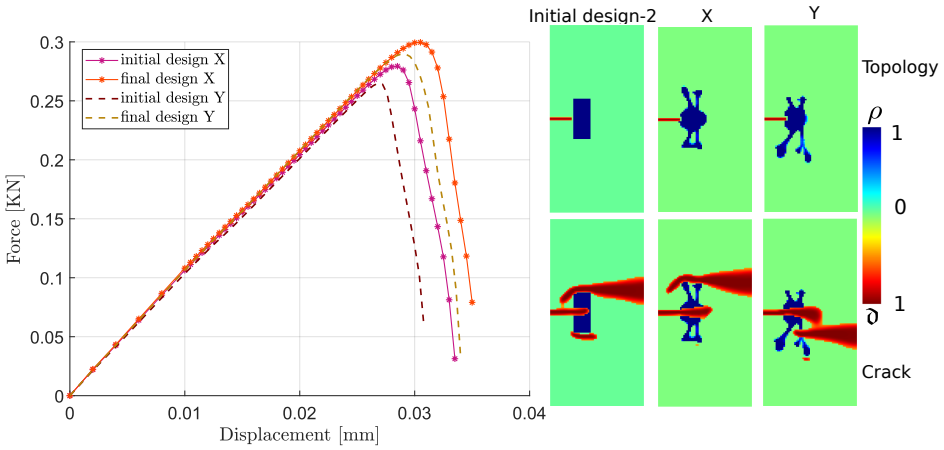

Figure 11: a) Force Vs. displacement of Design-2 with improved performance for Case-A, and b) Final optimum solution from the initial design along with the corresponding crack propagation.

It is evident that the optimum topology strongly depends on the primary: (i) elastic mismatch, as evidenced by the comparison of Case-A and Case-B, and (ii) inclusion mismatch and secondary apparent strength mismatch, as shown by the comparison of Case-B and Case-C.

4.2. Performance evaluation with an initial design guess

In this section, the improvement of fracture resistance in FGMs is evaluated by comparing an initial guess design to an optimized design in terms of load-carrying capacity. Note that, fracture resistance is directly proposed to load-carrying capacity. For the example of a notched plate, two initial guess designs are proposed, referred to as Design-1 and Design-2.

Design-1 consists of a horizontal block with a total volume fraction of the inclusion as $f^{inc} = 5\%$ located in front of the crack tip. This design increases the resistance to fracture in front of the crack tip and thus hinders crack propagation. Figure 10a) provides the force vs. displacement curve for the initial and final design for both grading directions in Case-A, while Figure 10b) provides the initial and final designs along with their respective crack propagation. It is noticed that for the grading in the x-direction, the load

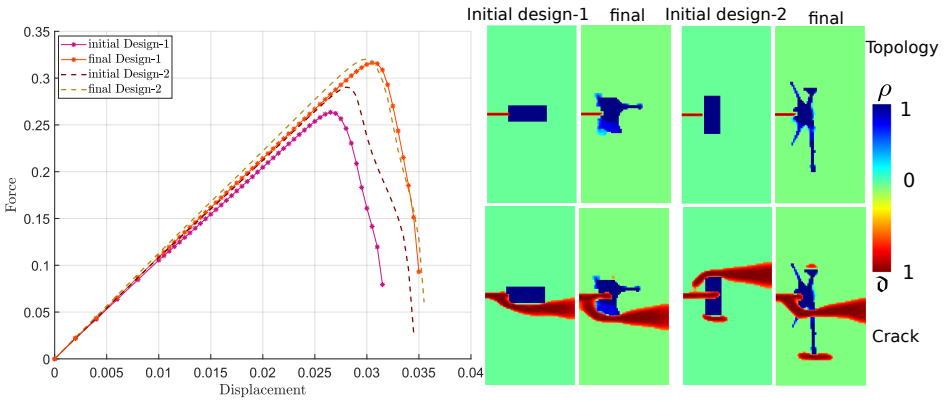

Figure 12: a) Force Vs. displacement of Design-1 and Design-2 with improved performance for Case-B, for grading in x-direction, and b) Final optimum solution from the initial design along with the corresponding crack propagation.

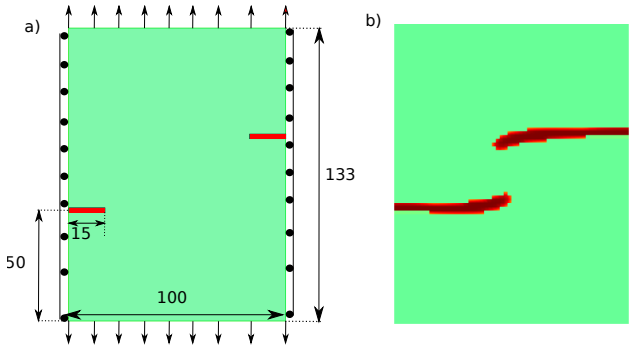

Figure 13: a) geometrical description of the asymmetrical notched specimen, b) crack propagation in the asymmetrical notch for homogeneous material medium.

carrying capacity of the specimen increases by 19.6070% from the initial design, whereas for the grading in the y-direction, the load carrying capacity increases by 25.9371%.

Design-2 consists of a vertical block with volume fraction of $f^{inc} = 5\%$ of inclusion material located in front of the crack tip, as shown in Figure 11b. The load carrying capacity of the specimen is increased by 7.2298% for grading in x-direction and 9.3620% for grading in y-direction, as observed from the Force vs. displacement curve provided in Figure 11a.

For Case-B, Figure 12 presents the initial guess and final optimized designs for the grading in x-direction. For Design-1, the load carrying capacity increases by 20.0759%, whereas for the initial guess of Design-2, load capacity increases by 10.3306%.

In conclusion, the proposed method shows significant improvement in fracture resistance with respect to the initial guess designs.

4.3. Asymmetrical Notch

With the analysis of the plate with notch at hand, this section presents an analysis of a plate with an asymmetrical notch containing two cracks, as illustrated in Figure 13 a). The plate has dimensions of $L = 133$ and $W = 100$, and is meshed with (80×60) elements of size $h_e = 1.66$ mm using the same conditions for ℓ, r_{min}, and the cracks condition as in the previous example.

Three cases are considered, using the same material properties as in the previous section, as shown in Table 1. It is worth noting that, in the case of a homogeneous material, crack propagation in such an

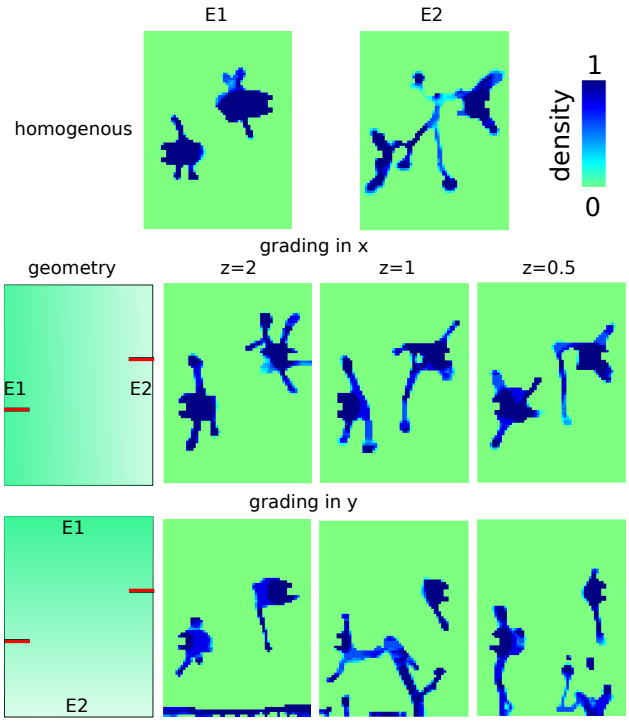

Figure 14: Grading in x direction for 10% volume fraction of inclusion for case-A

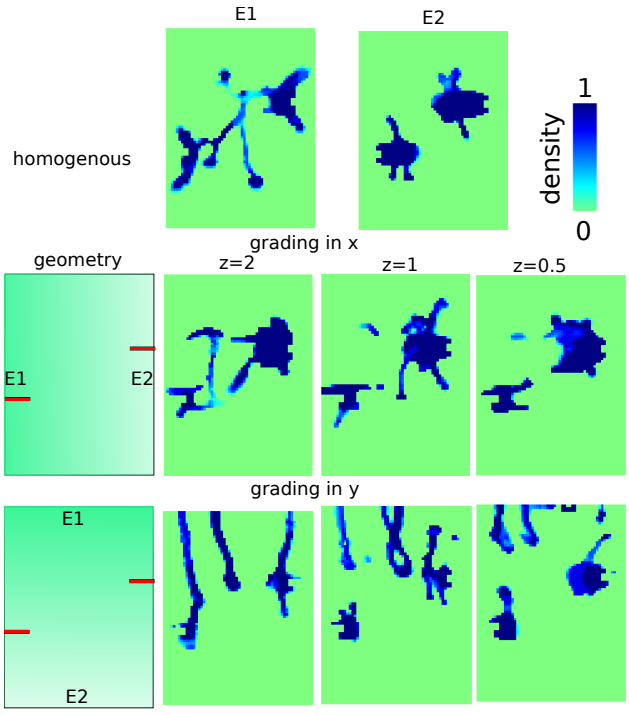

Figure 15: Grading in x direction for 10% volume fraction of inclusion for case-B

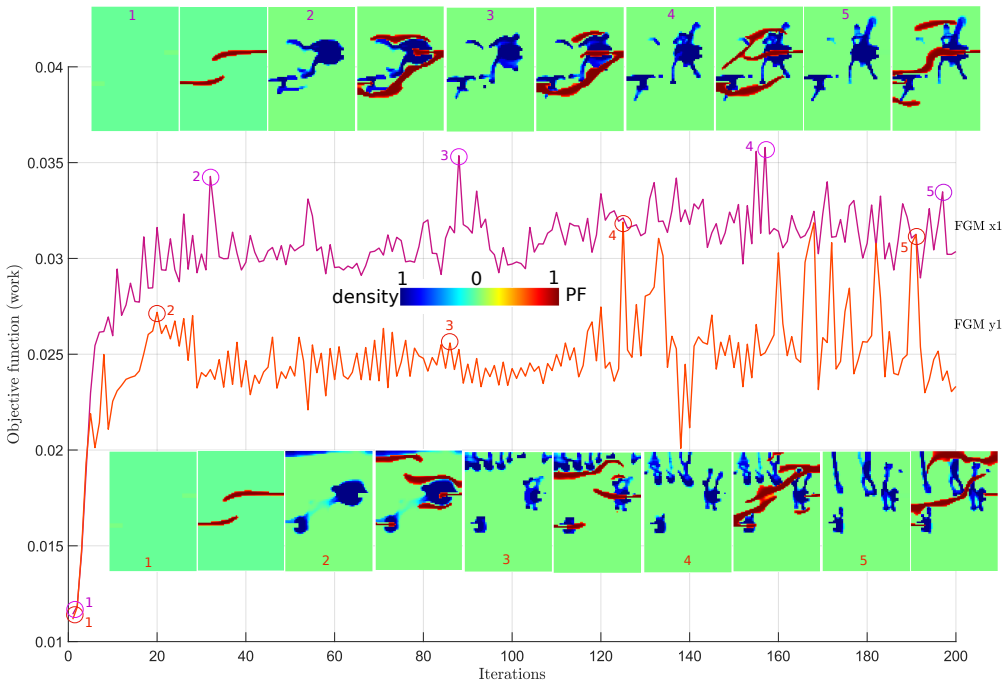

Figure 16: Evolution of the optimum topology in Case-B for the grading in X-direction and Y-direction for the volume fraction of 10% and $z = 1$.

asymmetrically notched specimen with two cracks is symmetrical, as depicted in Figure 13 b). However, in the cases where Functionally Graded Materials are used, one crack is dominant due to differences in material properties. As a result, the growth of one crack is faster than the other, resulting in asymmetrical crack growth.

Figure 14 presents the optimal solution for Case-A with $f^{inc} = 10\%$ for the variation of grading in the x- and y-directions with different z values. For Case-A, the fracture resistance decreases from E_1 to E_2 side, as shown in Figure 14. Therefore, crack propagation from the E_2 side is longer, and the optimal topology indicates that densities are concentrated towards E_2. For grading in the y-direction, both cracks tend to move towards the lowest Young's modulus (bottom), resulting in the densities being concentrated in the bottom half of the structure. It is worth noting that, for grading in both x- and y-directions, the optimal topology is sandwiched between its homogeneous surrogates.

Figure 15 shows the optimal solution for Case-B with $f^{inc} = 10\%$ for the variation of grading in the x- and y-directions at different z values, along with their corresponding homogeneous surrogates. In contrast to the notched plate, the work for FGM is bounded by its homogeneous constituents. This can be seen as a consequence of two stress concentration areas, where one area resists crack growth while the other promotes it, making the optimization problem harder. As a consequence, the densities are concentrated towards the right side due to the increased Young's modulus on that side for grading in the x-direction. On the other hand, for grading in the y-direction, the densities are concentrated on top due to the crack deflection towards the weaker E_1 (top) side.

Figure 16 demonstrates the crack evolution and optimum topology for Case-B with grading in x- and y-directions for $f^{inc} = 10\%$ and $z = 1$. The figure clearly displays the differences between homogeneous and FGM materials.

Figure 17 provides an overview of the optimal topologies for a volume fraction of $f^{inc} = 5\%$, along with their corresponding homogeneous surrogates, to exhibit the effects of elastic mismatch and inclusion mismatch for grading in the x- and y-directions. The material properties in line with Table 1 are $E_1 = 5.2$

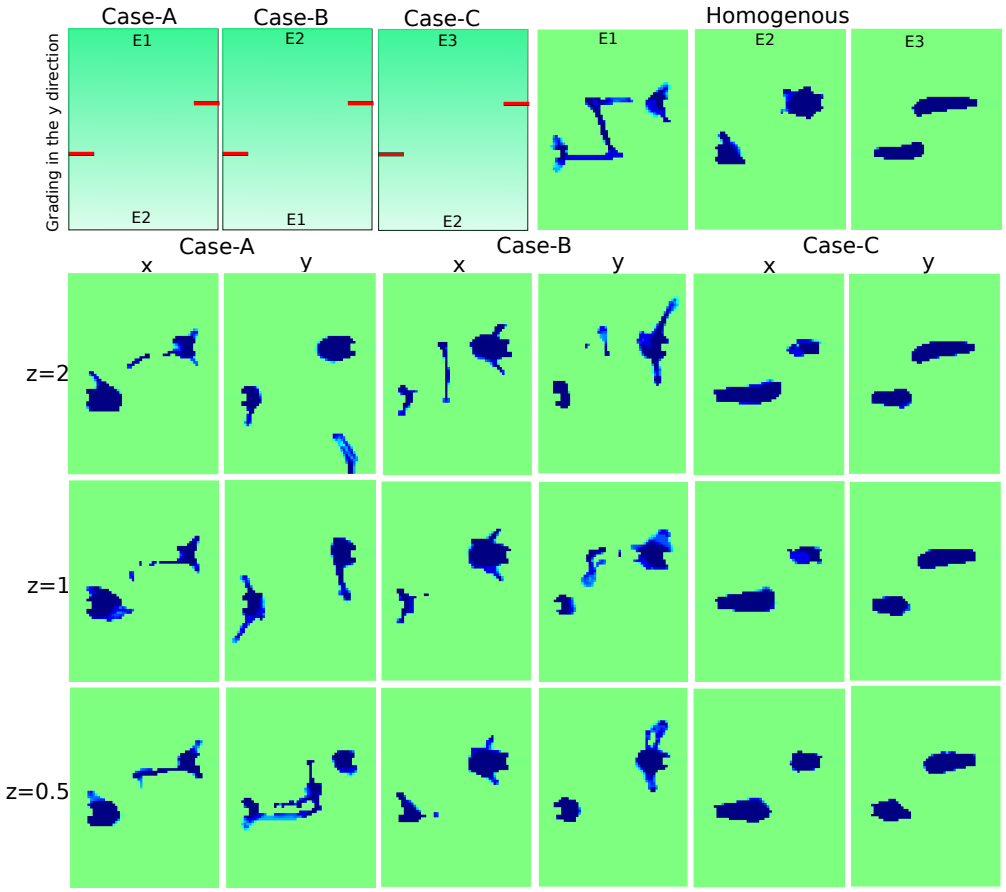

Figure 17: Overview of the optimum topologies for volume fraction of 5% for different cases and different z with $E1 = 5.2$, $E2 = 10.4$, and $E3 = 20.8$

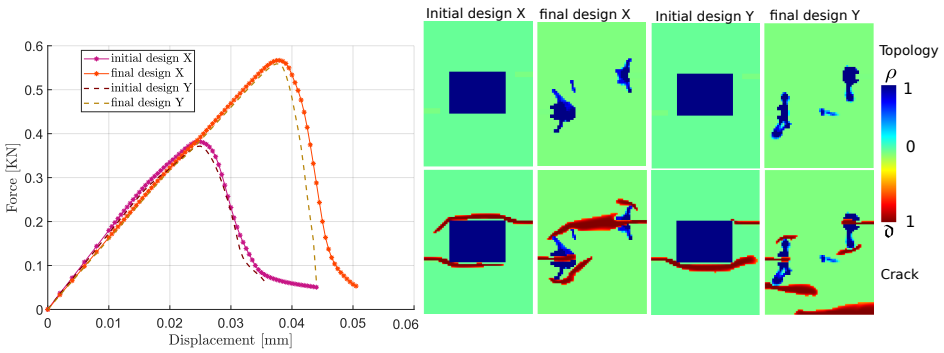

Figure 18: a) Force Vs. displacement with improved performance for Case-A, and b) Final optimum solution from the initial design along with the corresponding crack propagation.

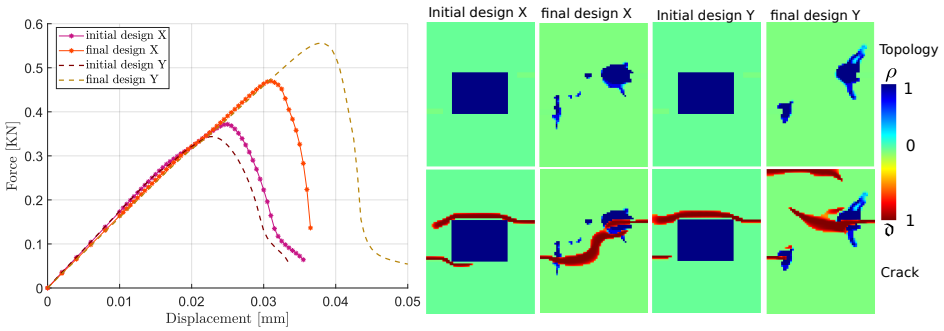

Figure 19: a) Force Vs. displacement with improved performance for Case-B, and b) Final optimum solution from the initial design along with the corresponding crack propagation.

GPa, $E_2 = 10.4$ GPa, and $E_3 = 20.8$ GPa. The difference in the elastic mismatch and inclusion mismatch can be clearly in comparison with the optimum solution of case-A and Case-C.

4.4. Performance assessment from an initial guess

Performance assessment based on the initial design

This section aims to evaluate the performance of topology optimization by comparing the final optimized design with the initial design guess for an asymmetrical notched specimen. The initial design guess considered in this study contains a block of inclusion material blocking both the crack tip and obstructing the crack propagation path entirely.

Figure 18 presents the Force vs. displacement curve for the grading in the x- and y-direction for Case-A, along with the initial guess design and final optimized designs, along with their crack propagation. The results indicate that the load-carrying capacity for grading in the x-direction and y-direction showed an improvement of 48.4332% and 50.3908%, respectively, compared to the initial guess design.

Similarly, for Case-B, the Force vs. displacement curve, along with the initial guess design and final optimized design, are presented in Figure. 19. The results show that the load-carrying capacity increases by 26.4289% for grading in the x-direction and 61.7192% for grading in the y-direction.

In conclusion, the results of this study indicate that topology optimization is effective in improving the load-carrying capacity of notched specimens in both x- and y-directions, as demonstrated by the significant improvement observed in the final optimized designs compared to the initial design guesses.

5. Conclusions

The article explores topology optimization in the context of functionally graded materials (FGMs) through two strategies. Firstly, it investigates topology optimization of compliance with FGM, emphasizing the design differences when considering FGM as the design material. This is achieved through various numerical examples. Secondly, it presents a SIMP topology optimization framework for maximizing fracture resistance in FGMs within the context of additive manufacturing.

The mathematical formalism is established by applying the variational method to fracture. Furthermore, $\Gamma-$convergence is established for every distribution of the density function, providing insights into the mechanical behavior of FGMs.

Through the minimization of compliance, the study reveals that compliance in FGMs is directly proportional to the Young's modulus ratio (elastic mismatch) and inversely proportional to the grading parameters when the Young's modulus ratio is greater than 1. Conversely, for Young's modulus ratios less than 1, compliance is directly proportional to the grading constant and inversely proportional to the elastic mismatch.

In the context of maximizing fracture resistance, the article presents two examples that showcase the effects of elastic mismatch, strength mismatch, inclusion mismatch, and inclusion strength mismatch, highlighting the differences between their homogeneous constituents. Detailed analyses of the optimum shapes are provided, and an improvement in performance compared to the initial designs is demonstrated, illustrating the capability of the model.

In conclusion, the article provides an overall assessment of FGMs in terms of minimizing compliance and maximizing fracture resistance, making them suitable for relevant applications in the industry.

6. Acknowledgement

JR and MP acknowledge the funding received from the Europen Union Horizon 2020 research and innovation program under the Marie Sklodowska-Curie Grant Agreement No. 101086342- Project DIAGONAL (Ductility and fracture toughness analysis of Functionally Graded Materials: HORIZON-MSCA-2021-SE-01 action).

References

[1] N. Rödel.J, Gradient materials: An overview of a novel concept, Zeit Metall 88: 358-71. (1997).
[2] Niino.M, Hirai.T, Watanabe.R, The functionally gradient materials, Jap Soc Compos Mat 13: 257-64. (1987).
[3] M. T. Tilbrook, Fatigue crack propagation in functionally graded materials, Ph.D. thesis, School of Materials Science & Engineering, University of New South Wales (2005).
[4] F. Delale, F. Erdogan, The Crack Problem for a Nonhomogeneous Plane, Journal of Applied Mechanics 50 (3) (1983) 609–614. doi:10.1115/1.3167098.
[5] N. Konda, F. Erdogan, The mixed mode crack problem in a nonhomogeneous elastic medium, Engineering Fracture Mechanics 47 (4) (1994) 533 – 545. doi:https://doi.org/10.1016/0013-7944(94)90253-4.
[6] F. Erdogan, Fracture mechanics of functionally graded materials, Composites Engineering 5 (7) (1995) 753 – 770. doi:https://doi.org/10.1016/0961-9526(95)00029-M.
[7] Z.-H. Jin, R. Batra, Some basic fracture mechanics concepts in functionally graded materials, Journal of the Mechanics and Physics of Solids 44 (8) (1996) 1221 – 1235. doi:https://doi.org/10.1016/0022-5096(96)00041-5.
[8] P. Gu, R. Asaro, Cracks in functionally graded materials, International Journal of Solids and Structures 34 (1) (1997) 1 – 17. doi:https://doi.org/10.1016/0020-7683(95)00289-8.
[9] P. Gu, R. Asaro, Crack deflection in functionally graded materials, International Journal of Solids and Structures 34 (24) (1997) 3085 – 3098. doi:https://doi.org/10.1016/S0020-7683(96)00175-8.
[10] J. Dolbow, J. Nadeau, On the use of effective properties for the fracture analysis of microstructured materials, Engineering Fracture Mechanics 69 (14) (2002) 1607 – 1634. doi:https://doi.org/10.1016/S0013-7944(02)00052-8.
[11] T. D. Ngo, A. Kashani, G. Imbalzano, K. T. Nguyen, D. Hui, Additive manufacturing (3d printing): A review of materials, methods, applications and challenges, Composites Part B: Engineering 143 (2018) 172–196. doi:https://doi.org/10.1016/j.compositesb.2018.02.012.
URL https://www.sciencedirect.com/science/article/pii/S1359836817342944
[12] M. P. Bendsøe, N. Kikuchi, Generating optimal topologies in structural design using a homogenization method, Computer Methods in Applied Mechanics and Engineering 71 (2) (1988) 197–224. doi:https://doi.org/10.1016/0045-7825(88)90086-2.
URL https://www.sciencedirect.com/science/article/pii/0045782588900862

[13] M. P. Bendsoe, Optimal shape design as a material distribution problem, Structural optimization 1 (4) (1989) 193–202. doi:10.1007/BF01650949.
URL https://doi.org/10.1007/BF01650949
[14] M. P. Bendsoe, O. Sigmund, Material interpolation schemes in topology optimization, Archive of Applied Mechanics 69 (9) (1999) 635–654. doi:10.1007/s004190050248.
URL https://doi.org/10.1007/s004190050248
[15] G. I. N. Rozvany, M. Zhou, T. Birker, Generalized shape optimization without homogenization, Structural optimization 4 (3) (1992) 250–252. doi:10.1007/BF01742754.
URL https://doi.org/10.1007/BF01742754
[16] M. Y. Wang, X. Wang, D. Guo, A level set method for structural topology optimization, Computer Methods in Applied Mechanics and Engineering 192 (1) (2003) 227–246. doi:https://doi.org/10.1016/S0045-7825(02)00559-5.
[17] G. Allaire, F. Jouve, A.-M. Toader, Structural optimization using sensitivity analysis and a level-set method, Journal of Computational Physics 194 (1) (2004) 363–393. doi:https://doi.org/10.1016/j.jcp.2003.09.032.
URL https://www.sciencedirect.com/science/article/pii/S002199910300487X
[18] P. Liu, Y. Luo, Z. Kang, Multi-material topology optimization considering interface behavior via xfem and level set method, Computer Methods in Applied Mechanics and Engineering 308 (2016) 113–133. doi:https://doi.org/10.1016/j.cma.2016.05.016.
URL https://www.sciencedirect.com/science/article/pii/S0045782516303802
[19] V. J. Challis, A discrete level-set topology optimization code written in Matlab, Structural and Multidisciplinary Optimization 41 (3) (2010) 453–464. doi:10.1007/s00158-009-0430-0.
URL https://doi.org/10.1007/s00158-009-0430-0
[20] Y. Xie, G. Steven, A simple evolutionary procedure for structural optimization, Computers Structures 49 (5) (1993) 885–896. doi:https://doi.org/10.1016/0045-7949(93)90035-C.
[21] J. D. Deaton, R. V. Grandhi, A survey of structural and multidisciplinary continuum topology optimization: post 2000, Structural and Multidisciplinary Optimization 49 (1) (2014) 1–38. doi:10.1007/s00158-013-0956-z.
URL https://doi.org/10.1007/s00158-013-0956-z
[22] O. Sigmund, K. Maute, Topology optimization approaches, Structural and Multidisciplinary Optimization 48 (6) (2013) 1031–1055. doi:10.1007/s00158-013-0978-6.
URL https://doi.org/10.1007/s00158-013-0978-6
[23] G. I. N. Rozvany, A critical review of established methods of structural topology optimization, Structural and Multidisciplinary Optimization 37 (3) (2009) 217–237. doi:10.1007/s00158-007-0217-0.
URL https://doi.org/10.1007/s00158-007-0217-0
[24] D. Yago, J. Cante, O. Lloberas-Valls, J. Oliver, Topology Optimization Methods for 3D Structural Problems: A Comparative Study, Archives of Computational Methods in Engineering 29 (3) (2022) 1525–1567. doi:10.1007/s11831-021-09626-2.
URL https://doi.org/10.1007/s11831-021-09626-2
[25] T. Sokol, A 99 line code for discretized Michell truss optimization written in Mathematica, Structural and Multidisciplinary Optimization 43 (2) (2011) 181–190. doi:10.1007/s00158-010-0557-z.
URL https://doi.org/10.1007/s00158-010-0557-z
[26] O. Sigmund, A 99 line topology optimization code written in Matlab, Structural and Multidisciplinary Optimization 21 (2) (2001) 120–127. doi:10.1007/s001580050176.
URL https://doi.org/10.1007/s001580050176
[27] E. Andreassen, A. Clausen, M. Schevenels, B. S. Lazarov, O. Sigmund, Efficient topology optimization in MATLAB using 88 lines of code, Structural and Multidisciplinary Optimization 43 (1) (2011) 1–16. doi:10.1007/s00158-010-0594-7.
URL https://doi.org/10.1007/s00158-010-0594-7
[28] K. Suresh, A 199-line Matlab code for Pareto-optimal tracing in topology optimization, Structural and Multidisciplinary Optimization 42 (5) (2010) 665–679. doi:10.1007/s00158-010-0534-6.
URL https://doi.org/10.1007/s00158-010-0534-6
[29] C. Talischi, G. H. Paulino, A. Pereira, I. F. M. Menezes, PolyMesher: a general-purpose mesh generator for polygonal elements written in Matlab, Structural and Multidisciplinary Optimization 45 (3) (2012) 309–328. doi:10.1007/s00158-011-0706-z.
URL https://doi.org/10.1007/s00158-011-0706-z
[30] K. A. James, H. Waisman, Failure mitigation in optimal topology design using a coupled nonlinear continuum damage model, Computer Methods in Applied Mechanics and Engineering 268 (2014) 614–631. doi:https://doi.org/10.1016/j.cma.2013.10.022.
URL https://www.sciencedirect.com/science/article/pii/S0045782513002740
[31] L. Li, G. Zhang, K. Khandelwal, Topology optimization of energy absorbing structures with maximum damage constraint, International Journal for Numerical Methods in Engineering 112 (7) (2017) 737–775. doi:https://doi.org/10.1002/nme.5531.
URL https://doi.org/10.1002/nme.5531
[32] L. Li, G. Zhang, K. Khandelwal, Failure resistant topology optimization of structures using nonlocal elastoplastic-damage model, Structural and Multidisciplinary Optimization 58 (4) (2018) 1589–1618. doi:10.1007/s00158-018-1984-5.
URL https://doi.org/10.1007/s00158-018-1984-5
[33] L. Li, K. Khandelwal, Design of fracture resistant energy absorbing structures using elastoplastic topology optimization, Structural and Multidisciplinary Optimization 56 (6) (2017) 1447–1475. doi:10.1007/s00158-017-1735-z.

URL https://doi.org/10.1007/s00158-017-1735-z
[34] Topology optimization of particle-matrix composites for optimal fracture resistance taking into account interfacial damage, International Journal for Numerical Methods in Engineering 115 (5) (2018) 604–626. arXiv:https://onlinelibrary.wiley.com/doi/pdf/10.1002/nme.5818, doi:https://doi.org/10.1002/nme.5818.
URL https://onlinelibrary.wiley.com/doi/abs/10.1002/nme.5818
[35] D. Da, J. Yvonnet, Topology optimization for maximizing the fracture resistance of periodic quasi-brittle composites structures, Materials 13 (15) (2020) 3279. doi:10.3390/ma13153279.
URL http://dx.doi.org/10.3390/ma13153279
[36] L. Xia, D. Da, J. Yvonnet, Topology optimization for maximizing the fracture resistance of quasi-brittle composites, Computer Methods in Applied Mechanics and Engineering 332 (2018) 234–254. doi:https://doi.org/10.1016/j.cma.2017.12.021.
URL https://www.sciencedirect.com/science/article/pii/S0045782517307715
[37] P. Li, Y. Wu, J. Yvonnet, A simp-phase field topology optimization framework to maximize quasi-brittle fracture resistance of 2d and 3d composites, Theoretical and Applied Fracture Mechanics 114 (2021) 102919. doi:https://doi.org/10.1016/j.tafmec.2021.102919.
URL https://www.sciencedirect.com/science/article/pii/S0167844221000276
[38] O. Amir, A topology optimization procedure for reinforced concrete structures, Computers Structures 114-115 (2013) 46–58. doi:https://doi.org/10.1016/j.compstruc.2012.10.011.
URL https://www.sciencedirect.com/science/article/pii/S0045794912002337
[39] J. Kato, E. Ramm, Multiphase layout optimization for fiber reinforced composites considering a damage model, Engineering Structures 49 (2013) 202–220. doi:https://doi.org/10.1016/j.engstruct.2012.10.029.
URL https://www.sciencedirect.com/science/article/pii/S0141029612005470
[40] C. F. Hilchenbach, E. Ramm, Optimization of multiphase structures considering damage, Structural and Multidisciplinary Optimization 51 (5) (2015) 1083–1096. doi:10.1007/s00158-014-1198-4.
URL https://doi.org/10.1007/s00158-014-1198-4
[41] V. J. Challis, A. P. Roberts, A. H. Wilkins, Fracture resistance via topology optimization, Structural and Multidisciplinary Optimization 36 (3) (2008) 263–271. doi:10.1007/s00158-007-0160-0.
URL https://doi.org/10.1007/s00158-007-0160-0
[42] Z. Kang, P. Liu, M. Li, Topology optimization considering fracture mechanics behaviors at specified locations, Structural and Multidisciplinary Optimization 55 (5) (2017) 1847–1864. doi:10.1007/s00158-016-1623-y.
URL https://doi.org/10.1007/s00158-016-1623-y
[43] O. Amir, O. Sigmund, Reinforcement layout design for concrete structures based on continuum damage and truss topology optimization, Structural and Multidisciplinary Optimization 47 (2) (2013) 157–174. doi:10.1007/s00158-012-0817-1.
URL https://doi.org/10.1007/s00158-012-0817-1
[44] P. K. Kristensen, C. F. Niordson, E. Martínez-Pañeda, An assessment of phase field fracture: crack initiation and growth, Philosophical Transactions of the Royal Society A: Mathematical, Physical and Engineering Sciences 379 (2203) (2021) 20210021. doi:10.1098/rsta.2021.0021.
[45] B. Bourdin, G. Francfort, J.-J. Marigo, Numerical experiments in revisited brittle fracture, Journal of the Mechanics and Physics of Solids 48 (4) (2000) 797 – 826. doi:https://doi.org/10.1016/S0022-5096(99)00028-9.
[46] M. Dittmann, F. Aldakheel, J. Schulte, P. Wriggers, C. Hesch, Variational phase-field formulation of non-linear ductile fracture, Computer Methods in Applied Mechanics and Engineering 342 (2018) 71 – 94. doi:https://doi.org/10.1016/j.cma.2018.07.029.
URL http://www.sciencedirect.com/science/article/pii/S0045782518303621
[47] C. Miehe, D. Kienle, F. Aldakheel, S. Teichtmeister, Phase field modeling of fracture in porous plasticity: A variational gradient-extended eulerian framework for the macroscopic analysis of ductile failure, Computer Methods in Applied Mechanics and Engineering 312 (2016) 3 – 50, phase Field Approaches to Fracture. doi:https://doi.org/10.1016/j.cma.2016.09.028.
URL http://www.sciencedirect.com/science/article/pii/S0045782516305412
[48] A. Dean, S. Sahraee, J. Reinoso, R. Rolfes, A new invariant-based thermo-plastic model for finite deformation analysis of short fibre reinforced composites: Development and numerical aspects, Composites Part B: Engineering 125 (2017) 241–258.
[49] R. Alessi, F. Freddi, Phase-field modelling of failure in hybrid laminates, Composite Structures 181 (2017) 9 – 25. doi:10.1016/j.compstruct.2017.08.073.
[50] J. Bleyer, R. Alessi, Phase-field modeling of anisotropic brittle fracture including several damage mechanisms, Computer Methods in Applied Mechanics and Engineering 336 (2018) 213 – 236. doi:https://doi.org/10.1016/j.cma.2018.03.012.
[51] A. Quintanas-Corominas, J. Reinoso, E. Casoni, A. Turon, J. Mayugo, A phase field approach to simulate intralaminar and translaminar fracture in long fiber composite materials, Composite Structures (2019). doi:10.1016/j.compstruct.2019.02.007.
[52] A. Dean, J. Reinoso, N. Jha, E. Mahdi, R. Rolfes, A phase field approach for ductile fracture of short fibre reinforced composites, Theoretical and Applied Fracture Mechanics 106 (2020) 102495. doi:https://doi.org/10.1016/j.tafmec.2020.102495.
URL http://www.sciencedirect.com/science/article/pii/S0167844219306536
[53] F. Alkhatib, E. Mahdi, A. Dean, Development of composite double-hat energy absorber device subjected to traverser loads, Composite Structures 240 (2020) 112046. doi:https://doi.org/10.1016/j.compstruct.2020.112046.
URL https://www.sciencedirect.com/science/article/pii/S0263822319345192

[54] M. Brod, A. Dean, S. Scheffler, C. Gerendt, R. Rolfes, Numerical modeling and experimental validation of fatigue damage in cross-ply cfrp composites under inhomogeneous stress states, Composites Part B: Engineering 200 (2020) 108050. doi:https://doi.org/10.1016/j.compositesb.2020.108050.
URL https://www.sciencedirect.com/science/article/pii/S1359836820306624
[55] P. Asur Vijaya Kumar, A. Dean, J. Reinoso, M. Paggi, A multi phase-field-cohesive zone model for laminated composites: Application to delamination migration, Composite Structures 276 (2021) 114471. doi:https://doi.org/10.1016/j.compstruct.2021.114471.
[56] A. Dean, P. Asur Vijaya Kumar, J. Reinoso, C. Gerendt, M. Paggi, E. Mahdi, R. Rolfes, A multi phase-field fracture model for long fiber reinforced composites based on the puck theory of failure, Composite Structures 251 (2020) 112446. doi:https://doi.org/10.1016/j.compstruct.2020.112446.
[57] E. Martínez-Pañeda, A. Golahmar, C. F. Niordson, A phase field formulation for hydrogen assisted cracking, Computer Methods in Applied Mechanics and Engineering 342 (2018) 742 – 761. doi:https://doi.org/10.1016/j.cma.2018.07.021.
URL http://www.sciencedirect.com/science/article/pii/S0045782518303529
[58] M. Isfandbod, E. Martínez-Pañeda, A mechanism-based multi-trap phase field model for hydrogen assisted fracture, International Journal of Plasticity 144 (2021) 103044. doi:https://doi.org/10.1016/j.ijplas.2021.103044.
[59] C. Schreiber, R. Müller, C. Kuhn, Phase field simulation of fatigue crack propagation under complex load situations, Archive of Applied Mechanics 91 (2) (2021) 563–577. doi:10.1007/s00419-020-01821-0.
[60] K. Seleš, F. Aldakheel, Z. Tonković, J. Sorić, P. Wriggers, A general phase-field model for fatigue failure in brittle and ductile solids, Computational Mechanics 67 (5) (2021) 1431–1452. doi:10.1007/s00466-021-01996-5.
[61] P. Carrara, M. Ambati, R. Alessi, L. De Lorenzis, A framework to model the fatigue behavior of brittle materials based on a variational phase-field approach, Computer Methods in Applied Mechanics and Engineering 361 (2020) 112731. doi:https://doi.org/10.1016/j.cma.2019.112731.
[62] Z. Khalil, A. Y. Elghazouli, E. Martínez-Pañeda, A generalised phase field model for fatigue crack growth in elastic–plastic solids with an efficient monolithic solver, Computer Methods in Applied Mechanics and Engineering 388 (2022) 114286. doi:https://doi.org/10.1016/j.cma.2021.114286.
[63] R. G. Tangella, P. Kumbhar, R. K. Annabattula, Hybrid phase-field modeling of thermo-elastic crack propagation, International Journal for Computational Methods in Engineering Science and Mechanics 0 (0) (2021) 1–16. doi:10.1080/15502287.2021.1904462.
[64] H. Badnava, M. A. Msekh, E. Etemadi, T. Rabczuk, An h-adaptive thermo-mechanical phase field model for fracture, Finite Elements in Analysis and Design 138 (2018) 31–47. doi:https://doi.org/10.1016/j.finel.2017.09.003.
[65] T.-T. Nguyen, D. Waldmann, T. Q. Bui, Computational chemo-thermo-mechanical coupling phase-field model for complex fracture induced by early-age shrinkage and hydration heat in cement-based materials, Computer Methods in Applied Mechanics and Engineering 348 (2019) 1–28. doi:https://doi.org/10.1016/j.cma.2019.01.012.
[66] P. K. Asur Vijaya Kumar, A. Dean, J. Reinoso, M. Paggi, Thermo-elastic solid shell formulation with phase field fracture for thin-walled fgms, Thin-Walled Structures 179 (2022) 109535. doi:https://doi.org/10.1016/j.tws.2022.109535.
URL https://www.sciencedirect.com/science/article/pii/S026382312200355X
[67] P. K. A. V. Kumar, A. Dean, S. Sahraee, J. Reinoso, M. Paggi, Non-linear thermoelastic analysis of thin-walled structures with cohesive-like interfaces relying on the solid shell concept, Finite Elements in Analysis and Design 202 (2022) 103696. doi:https://doi.org/10.1016/j.finel.2021.103696.
[68] P. K. Asur Vijaya Kumar, A. Dean, J. Reinoso, M. Paggi, Nonlinear thermo-elastic phase-field fracture of thin-walled structures relying on solid shell concepts, Computer Methods in Applied Mechanics and Engineering 396 (2022) 115096. doi:https://doi.org/10.1016/j.cma.2022.115096.
[69] P. Asur Vijaya Kumar, A. Dean, J. Reinoso, P. Lenarda, M. Paggi, Phase field modeling of fracture in functionally graded materials:γ-convergence and mechanical insight on the effect of grading, Thin-Walled Structures 159 (2021) 107234. doi:https://doi.org/10.1016/j.tws.2020.107234.
URL https://www.sciencedirect.com/science/article/pii/S0263823120311046
[70] Hirshikesh, S. Natarajan, R. K. Annabattula, E. Martínez-Pañeda, Phase field modelling of crack propagation in functionally graded materials, Composites Part B: Engineering 169 (2019) 239–248. doi:https://doi.org/10.1016/j.compositesb.2019.04.003.
URL https://www.sciencedirect.com/science/article/pii/S135983681930229X
[71] J.-Y. Wu, V. P. Nguyen, C. T. Nguyen, D. Sutula, S. Sinaie, S. P. Bordas, Chapter one - phase-field modeling of fracture, Vol. 53 of Advances in Applied Mechanics, Elsevier, 2020, pp. 1–183. doi:https://doi.org/10.1016/bs.aams.2019.08.001.
URL https://www.sciencedirect.com/science/article/pii/S0065215619300134
[72] D. Da, X. Qian, Fracture resistance design through biomimicry and topology optimization, Extreme Mechanics Letters 40 (2020) 100890. doi:https://doi.org/10.1016/j.eml.2020.100890.
[73] X. Huang, Y. Xie, Convergent and mesh-independent solutions for the bi-directional evolutionary structural optimization method, Finite Elements in Analysis and Design 43 (14) (2007) 1039–1049.
[74] M. P. Bendsøe, Optimal shape design as a material distribution problem, Structural optimization 1 (4) (1989) 193–202.
[75] J. B. Russ, H. Waisman, Topology optimization for brittle fracture resistance, Computer Methods in Applied Mechanics and Engineering 347 (2019) 238–263. doi:https://doi.org/10.1016/j.cma.2018.12.031.
URL https://www.sciencedirect.com/science/article/pii/S0045782518306303
[76] J. B. Russ, H. Waisman, A novel topology optimization formulation for enhancing fracture resistance with a single quasi-brittle material, International Journal for Numerical Methods in Engineering 121 (13) (2020) 2827–2856. doi:https://doi.org/10.1002/nme.6334.

URL https://onlinelibrary.wiley.com/doi/abs/10.1002/nme.6334
[77] C. Wu, J. Fang, S. Zhou, Z. Zhang, G. Sun, G. P. Steven, Q. Li, Level-set topology optimization for maximizing fracture resistance of brittle materials using phase-field fracture model, International Journal for Numerical Methods in Engineering 121 (13) (2020) 2929–2945. doi:https://doi.org/10.1002/nme.6340.
URL https://onlinelibrary.wiley.com/doi/abs/10.1002/nme.6340
[78] B. San, H. Waisman, Optimization of Carbon Black Polymer Composite Microstructure for Rupture Resistance, Journal of Applied Mechanics 84 (2), 021005 (11 2016). doi:10.1115/1.4035050.
URL https://doi.org/10.1115/1.4035050
[79] N. Noii, H. A. Jahangiry, H. Waisman, Level-set topology optimization for ductile and brittle fracture resistance using the phase-field method, Computer Methods in Applied Mechanics and Engineering 409 (2023) 115963. doi:https://doi.org/10.1016/j.cma.2023.115963.
URL https://www.sciencedirect.com/science/article/pii/S0045782523000865
[80] L. Ambrosio, V. M. Tortorelli, Approximation of functional depending on jumps by elliptic functional via γ-convergence, Communications on Pure and Applied Mathematics 43 (8) 999–1036. doi:10.1002/cpa.3160430805.
[81] A. Chambolle, V. Crismale, Compactness and lower semicontinuity in *gsbd* (2018). arXiv:1802.03302.
[82] C. Chambolle, A., A density result in gsbdp with applications to the approximation of brittle fracture energies., Arch Rational Mech Anal 232, (2019) 1329–1378doi:https://doi.org/10.1007/s00205-018-01344-7.
[83] A. Chambolle, An approximation result for special functions with bounded deformation, Journal de Mathématiques Pures et Appliquées 83 (7) (2004) 929 – 954. doi:https://doi.org/10.1016/j.matpur.2004.02.004.
URL http://www.sciencedirect.com/science/article/pii/S0021782404000285
[84] A. Chambolle, S. Conti, G. A. Francfort, Approximation of a Brittle Fracture Energy with a Constraint of Non-interpenetration, Archive for Rational Mechanics and Analysis 228 (3) (2018) 867–889. doi:10.1007/s00205-017-1207-z.
URL https://doi.org/10.1007/s00205-017-1207-z
[85] L. Ambrosio, A. Coscia, G. D. Maso, Fine properties of functions with bounded deformation, Arch. Rational Mech. Anal. 139 (1997) 201–238.
[86] S. Semmes, Some elementary aspects of hausdorff measure and dimension (2010). arXiv:1008.2637.

7. Appendix

7.1. Half Three-point bending with Hole

Material properties considered
$E_1 = 210$, $E_2 = E_1 * \mathcal{R}$, volume $f = 50\%$, $R_{min} = 4$ and the grading profile is defined as

$$E(\mathbf{x}) = E_1 + (E_2 - E_1) * V_f(\mathbf{x}); \quad V_f = \left(\frac{x}{h}\right)^z \tag{61}$$

where z is the grading constant. The variation of optimum design for the grading in the x-direction is presented in Fig. 20, and the grading in the y-direction is presented in Fig. 21. The pictures are self-explanatory and hence the analysis is omitted here for the sake of brevity.

7.2. Multi-Objective Optimisation

Material properties considered
$E_1 = 210$, $E_2 = E_1 * \mathcal{R}$, volume $f = 40\%$, $R_{min} = 6$ and the grading profile is defined as

$$E(\mathbf{x}) = E_1 + (E_2 - E_1) * V_f(\mathbf{x}); \quad V_f = \left(\frac{x}{h}\right)^z \tag{62}$$

where z is the grading constant. The variation of optimum design for the grading in the x-direction and y-direction is presented in Fig. 24, The pictures are self-explanatory and hence the analysis is omitted here for the sake of brevity.

8. Plate with notch: Results for Case-C

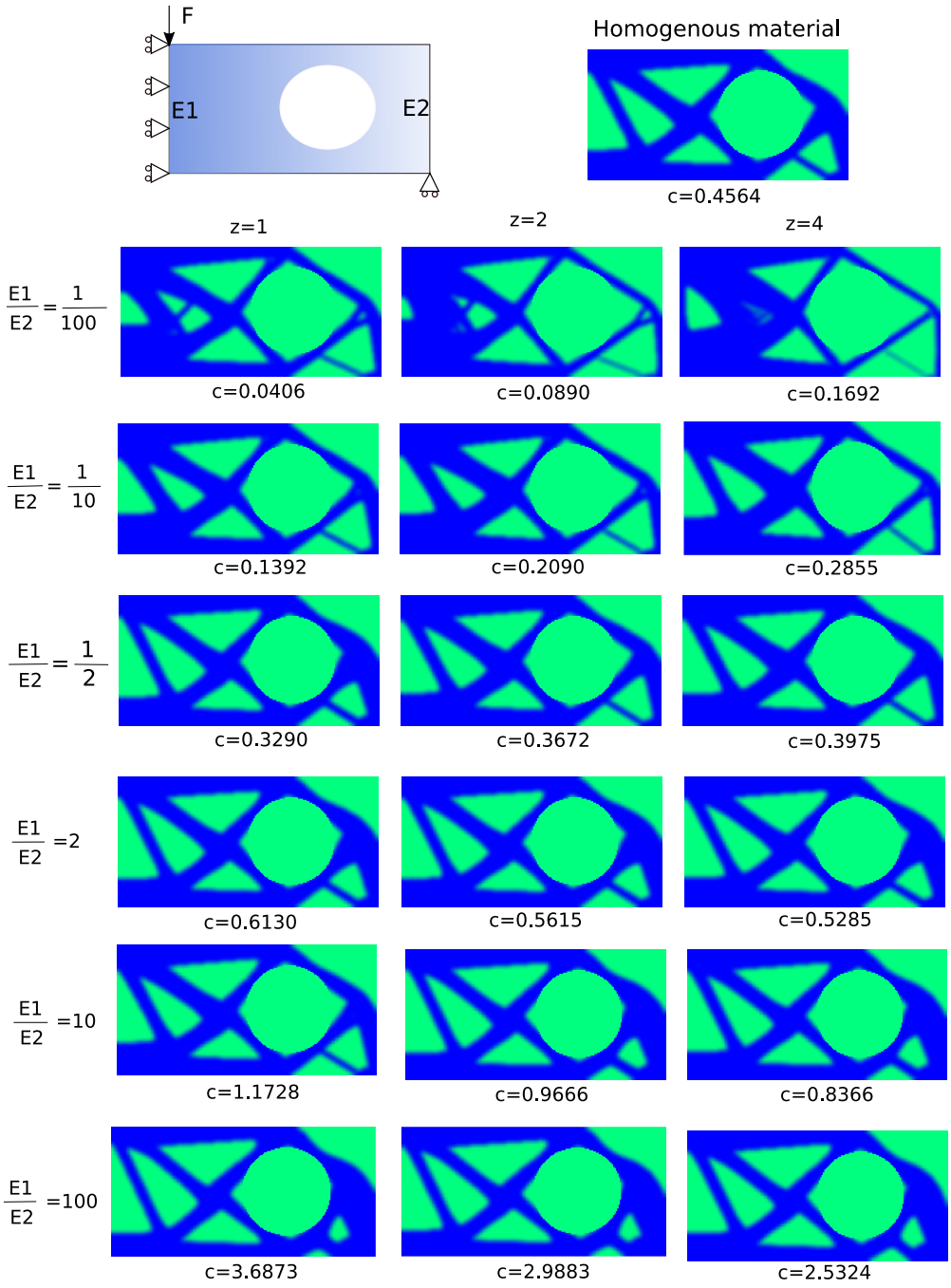

Figure 20: The Design domain, boundary conditions, external load for optimization of a symmetric MBB beam with a hole along with the optimized design for FGM with grading in the x-direction for different grading profiles.

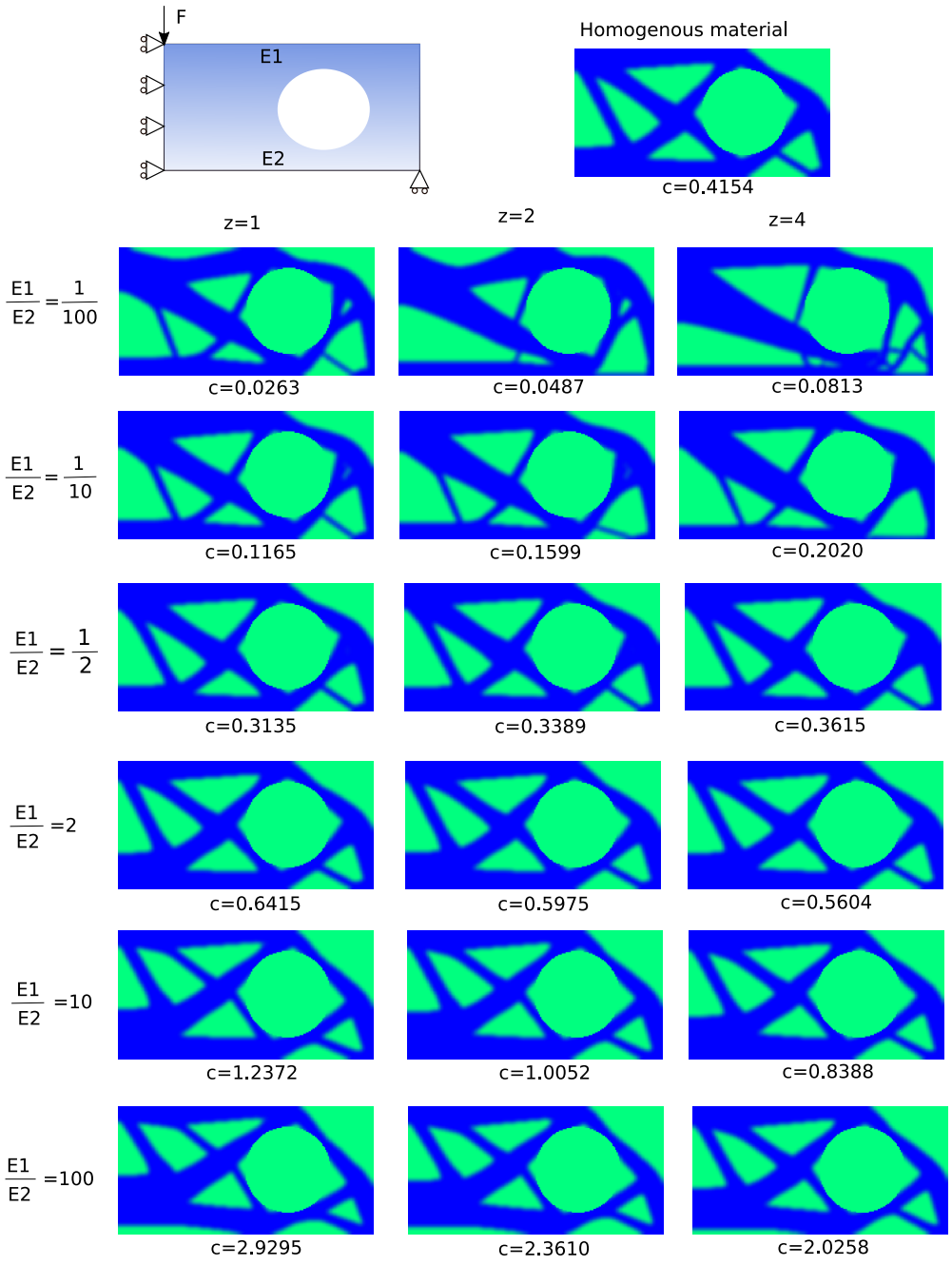

Figure 21: The Design domain, boundary conditions, external load for optimization of a symmetric MBB beam with a hole along with the optimized design for FGM with grading in y-direction for different grading profiles.

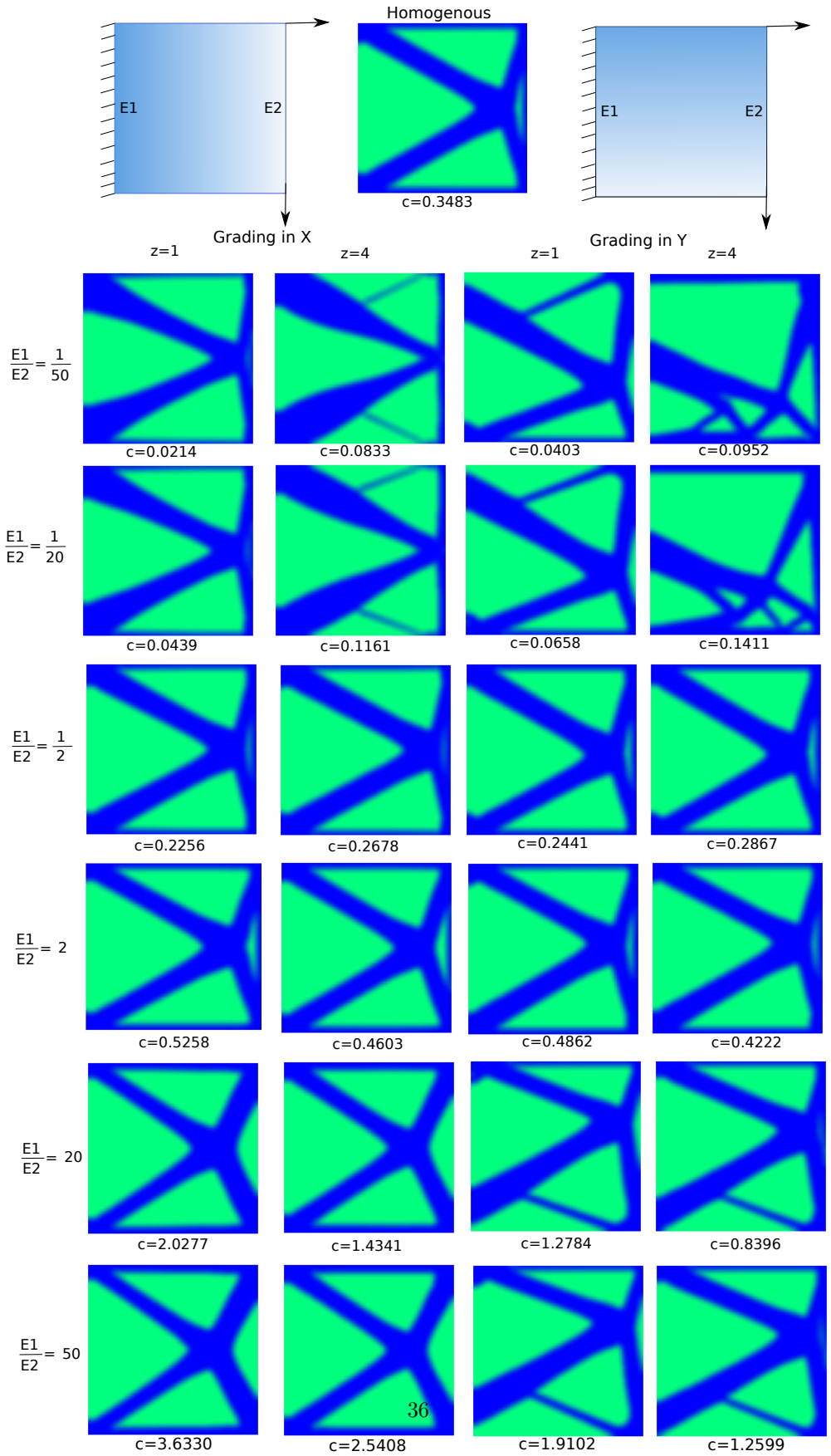

Figure 22: The Design domain, boundary conditions, external load for optimization of a cantilever beam with two load cases, and the optimized design for FGM with grading in x-direction and y-direction (separately) for different grading profiles.

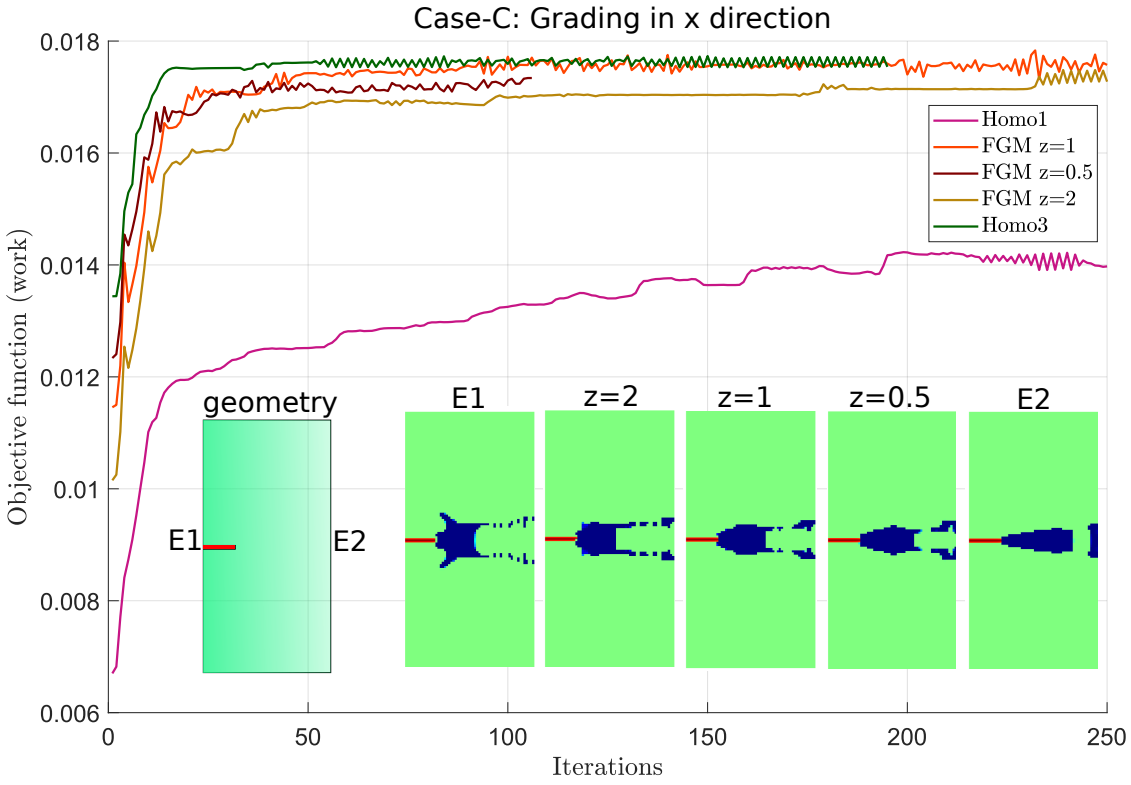

Figure 23: Grading in the x-direction for 5 percent volume fraction of inclusion for Case-C

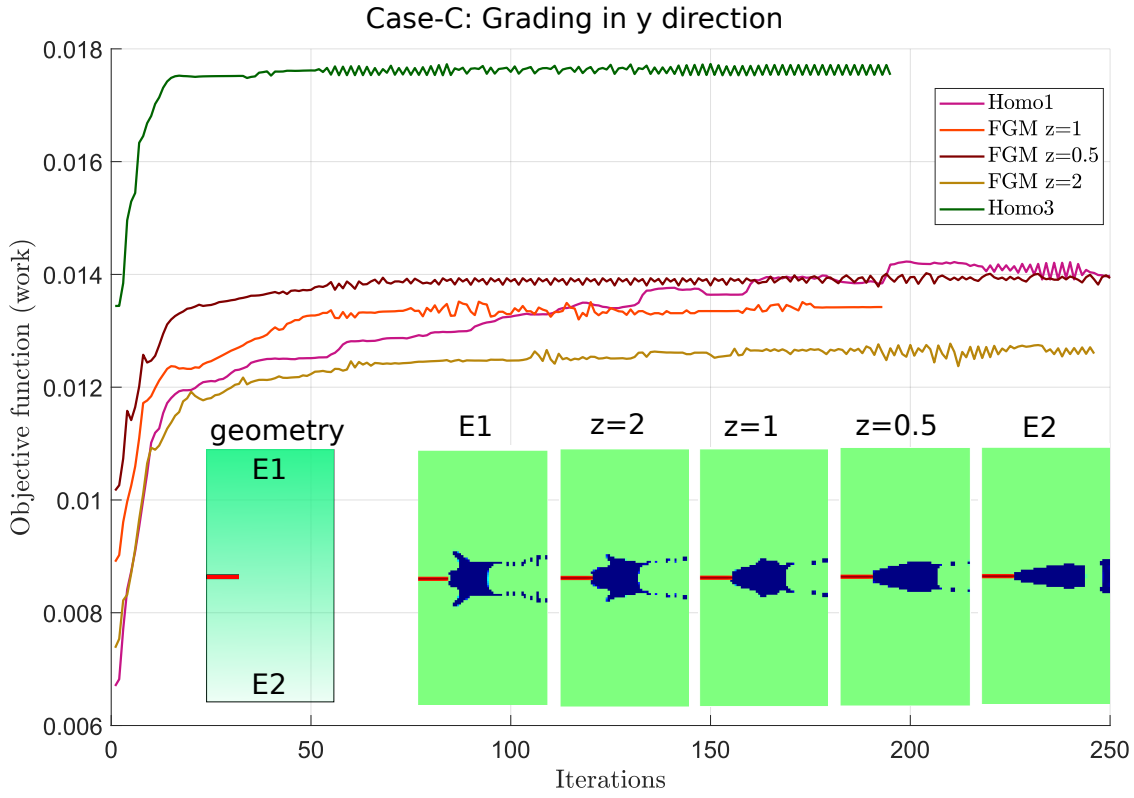

Figure 24: Grading in y-direction for 5 percent volume fraction of inclusion for Case-C